Petroleum Science 23 (2026) 7538–7560

Contents lists available at ScienceDirect

Petroleum Science

journal homepage: www.keaipublishing.com/en/journals/petroleum-science

Original Paper

Creep properties of fractured hydrate-bearing sediments

Lei Wang [a,c], Jia-Hao Yu [a,c], Kai Zhang [a,b,*], Zhi-Heng Liu [a], Wen-Qi Yu [a,c], Zhao-Ran Wu [a,**], Jing-Yan Lan [a,c], Qiang Wang [a], Bing-Bing Chen [d]

[a] State Key Laboratory of Metastable Materials Science and Technology, Yanshan University, Qinhuangdao, 066004, Hebei, China
[b] State Key Laboratory of Coal Mine Disaster Dynamics and Control, Chongqing University, Chongqing, 400044, China
[c] Hebei Key Laboratory of Green Construction and Intelligent Maintenance for Civil Engineering, Yanshan University, Qinhuangdao, 066004, Hebei, China
[d] Key Laboratory of Ocean Energy Utilization and Energy Conservation of Ministry of Education, Dalian University of Technology, Dalian, 116024, Liaoning, China

ARTICLE INFO

Article history:
Received 13 September 2025
Received in revised form
21 January 2026
Accepted 8 April 2026
Available online 14 April 2026

Edited by Min Li

Keywords:
Fracture
Creep properties
Hydrate-bearing sediments

ABSTRACT

Long-term extraction of natural gas hydrates can induce reservoir creep, leading to geological hazards such as submarine landslides and wellbore instability. The presence of widespread natural fractures can intensify this creep deformation by altering stress distributions, thereby significantly increasing engineering geological risks. However, the influence of key parameters on the creep behaviour of fractured hydrate-bearing sediments remains insufficiently understood. This study presents a systematic investigation into the creep properties of fractured and fracture-free hydrate-bearing sediments under various conditions, including effective confining pressures and hydrate saturations. It provides a reference for assessing the stability of fractured hydrate-bearing reservoirs. A comparative analysis of total creep strain, attenuation-creep strain, and rheological rate was conducted to elucidate the distinct mechanical responses of the two types of sediments. The results reveal that fractures fundamentally alter the sediment's creep behaviour. In fractured sediments, key creep parameters exhibit a non-monotonic dependence on hydrate saturation, with total creep strain peaking at a critical saturation of approximately 20%. In contrast, the same parameters in fracture-free sediments show a consistent positive correlation with hydrate saturation. For both sediment types, the rheological initiation time increases with both effective confining pressures and hydrate saturation, indicating this relationship is independent of fracturing. Crucially, the total creep strain is predominantly governed by the attenuation-creep stage, regardless of fracture presence. This work improves the understanding of creep mechanics in fractured hydrate reservoirs and provides a critical theoretical basis for engineering geological safety assessments and the optimisation of hydrate extraction strategies.
© 2026 Publishing services by Elsevier B.V. on behalf of KeAi Communications Co. Ltd. This is an open access article under the CC BY-NC-ND license (http://creativecommons.org/licenses/by-nc-nd/4.0/).

1. Introduction

Natural gas hydrates (NGHs) are clathrate crystals with a widespread global distribution (Chen et al., 2026; Zhang et al. 2024b, 2025). Their complete combustion would release energy roughly equivalent to that from burning all other existing fossil fuels combined (Zhang et al., 2024c). Their vast reserves and clean-burning nature make them a promising clean energy source with immense potential (Wu et al., 2025; Yang et al., 2026). However, during NGH extraction, hydrate decomposition releases significant amounts of free gas and water, triggering a redistribution of reservoir stresses (Chen et al., 2025; Jiang et al., 2015; Tan et al., 2021). Furthermore, hydrate decomposition reduces intergranular cementation within the reservoir, thereby diminishing its strength and stability. This process may induce marine engineering geological hazards, such as reservoir instability and submarine landslides (Dong et al., 2024). Therefore, it is essential to investigate the mechanical properties of the reservoir during NGH extraction to ensure reservoir stability and the safety of extraction operations (Zhang et al., 2026).

In recent years, numerous scholars have researched the mechanical behaviours of hydrate-bearing sediments (HBSs) under varying influencing factors to ensure the engineering geological

* Corresponding author.
** Corresponding author.
E-mail addresses: ZK20221101@163.com (K. Zhang), wuzhaoran@ysu.edu.cn (Z.-R. Wu).
Peer review under the responsibility of China University of Petroleum (Beijing).

https://doi.org/10.1016/j.petsci.2026.04.010
1995-8226/© 2026 Publishing services by Elsevier B.V. on behalf of KeAi Communications Co. Ltd. This is an open access article under the CC BY-NC-ND license (http://creativecommons.org/licenses/by-nc-nd/4.0/).

safety of reservoirs. Priest and Hayley (2019) studied the strength characteristics of hydrated sand and its relationship with natural hydrated sediments. The results showed that both laboratory-synthesized and naturally hydrated sands exhibited a "cemented" morphology, and their friction angles and cohesion are strongly influenced by the hydrate morphology, sample disturbance, and testing conditions. You et al. (2023) conducted drained triaxial compression experiments to investigate the strength properties of hydrate reservoirs under gas saturation and water saturation conditions. Their results showed that the failure strength of the specimens under excess gas conditions was controlled by the cementation component, whereas under excess water conditions, it was controlled by the frictional component. Zhang et al. (2024a) performed a series of triaxial shear tests on pore-filling HBSs, with results revealing that the shear strength of the sediments increased uniformly with increasing hydrate saturation (HS). They found that pore-filling hydrates enhanced the strength of the sediments by improving the frictional properties between the material constituents. Li et al. (2021) investigated the effect of hydrate occurrence patterns on the mechanical behaviour of sediments. The results indicated that the type of deviatoric stress-strain curve (strain-softening or strain-hardening) during shearing depends on the layer with the lowest HS. Moreover, the inclusion of such a layer was found to reduce the overall strength of the sediments. Du et al. (2023) prepared hydrate layers with different thicknesses and angles to analyse the effect of hydrate layer geometry on the strength properties of the reservoir. Their results showed that increasing the thickness of the hydrate layer increased the cohesion and the angle of internal friction of the specimen, while the angle of the hydrate layer affected the contact between the hydrate-bearing and hydrate-free layers, which in turn influenced the mechanical properties of the reservoir. Sang et al. (2025) noted that the layered distribution of NGHs impacts the mechanical properties of HBSs, conducted a series of consolidated-drained triaxial shear tests. Their results indicated that an increase in HS in the upper layer increased the failure strength, stiffness, and cohesion of the sediments, while having a relatively minor influence on the internal friction angle. Liu et al. (2021) used resonant column tests to systematically evaluate key mechanical parameters such as shear modulus and damping ratio. The results showed that the normalised modulus of highly saturated specimens decreases abruptly and the damping ratio increases dramatically under strain, implying a high sensitivity of reservoir mechanical properties to hydrate saturation during the extraction process. Li et al. (2025b) investigated reservoir seepage characteristics using a custom-designed multi-phase seepage experimental system. The results showed that the blocking effect of multiphase fluids affects the migration of water more than that of gas, and that specimens with larger porosity showed better fluid flow recovery. Evidently, factors such as the three-phase distribution within the sediment and the occurrence form of hydrates have differing impacts on the mechanical properties of the reservoir. Understanding the resulting evolution of these mechanical properties is central to addressing engineering geological issues in NGH exploitation projects. However, current research on the mechanical properties of HBSs predominantly centres on static mechanical properties such as shear strength and elastic modulus, while relatively little attention has been given to their long-term creep behaviour.

Creep characteristics are a key consideration in the study of engineering geological problems. Long-term extraction of NGHs can induce creep deformation in the reservoir. For instance, free gas generated from hydrate decomposition may accumulate in localised areas, leading to overpressure (Chen et al., 2023; Liu et al., 2020). Additionally, the weakening of cementation can disrupt the stress distribution within the reservoir by affecting its internal structure. Both of these factors can induce creep. The resulting reservoir creep deformation is a primary cause of geological hazards such as sand production, wellbore instability, and submarine landslides during long-term NGH extraction (Zhou et al., 2015). Preventing these engineering geological disasters is an essential consideration for NGHs exploitation projects. Fig. 1 presents a schematic diagram illustrating the triggers of creep and the geological hazards it can induce. The decomposition of natural gas hydrates causes higher-pressure gas to appear locally in the reservoir, weakens the originally existing cementation, and causes displacement of soil particles. This will induce uneven local stress in the reservoir and lead to creep. Under long-term action, obvious stress differences emerged in the entire reservoir, leading to the occurrence of disasters.

Therefore, studying the creep properties of NGH reservoirs is of vital importance. Several studies have begun to explore these time-dependent properties. Cai et al. (2020) proposed a classification model by using computed tomography imaging technology and combining with the water flow experiment of clay-silty samples to explain the influence of axial stress and creep microstructure on the permeability of natural gas hydrate reservoirs. Considering the possible coexistence of NGHs and ice, Li et al. (2016) investigated the creep properties of hydrate-ice specimens. Their conclusions indicate that the axial strain of the specimens increases with decreasing confining pressure (CP) and increasing temperature. The creep strain rate exhibits a negative correlation with CP and initially increases then decreases with rising temperature. To address this time-dependent deformation behaviour of the near-wellbore formation, study by Li et al. (2024) applied outward lateral stresses to HBSs to simulate the horizontal stress state of the near-wellbore reservoir. The results indicate that, before the effective stress reaches the long-term strength, decelerating creep accounts for more than 70% of the lateral strain. Hu et al. (2025) investigated the creep properties of HBSs during a loading-unloading process. Their results demonstrate that lower stress recovery in the unloading state leads to specimen compaction. However, when the stress recovery reaches a certain threshold, it results in an increase in creep strain. Liu et al. (2024) studied the creep properties of HBSs using clay-silt sediments as specimens, with results indicating that these HBSs exhibit typical steady creep behaviour, and that the creep and volumetric strain of the sediments show a positive correlation with the stress ratio and effective confining pressure (ECP). Wang et al. (2025a) performed a series of triaxial shear and creep experiments on over-consolidated HBSs. The results reveal that, under the same constant load and HS, an increase in the over-consolidation ratio leads to a decrease in creep deformation and creep rate. Furthermore, when there are significant differences in failure strength caused by varying over-consolidation ratios and HS, the creep deformation and creep rate are solely related to the constant load. This body of research demonstrates that understanding the creep characteristics of reservoirs during the NGH extraction is key to addressing the associated engineering geological challenges.

Moreover, fractures are widely distributed in submarine HBSs (Li et al., 2023b). The influence of these fractures on the reservoir structure is an important aspect of studying the engineering geological issues of hydrate reservoirs. Hydrates typically develop within fractures in nodular, vein-like, laminated, and massive forms (Li et al., 2022). Table 1 presents the distribution of fractures in global hydrate reservoirs. The presence of fractures and the unique state of hydrate occurrence within them endow fractured hydrate-bearing sediments (FHBSs) with mechanical properties distinct from those of fracture-free hydrate-bearing sediments (FFHBSs). This distinction may exacerbate creep deformation

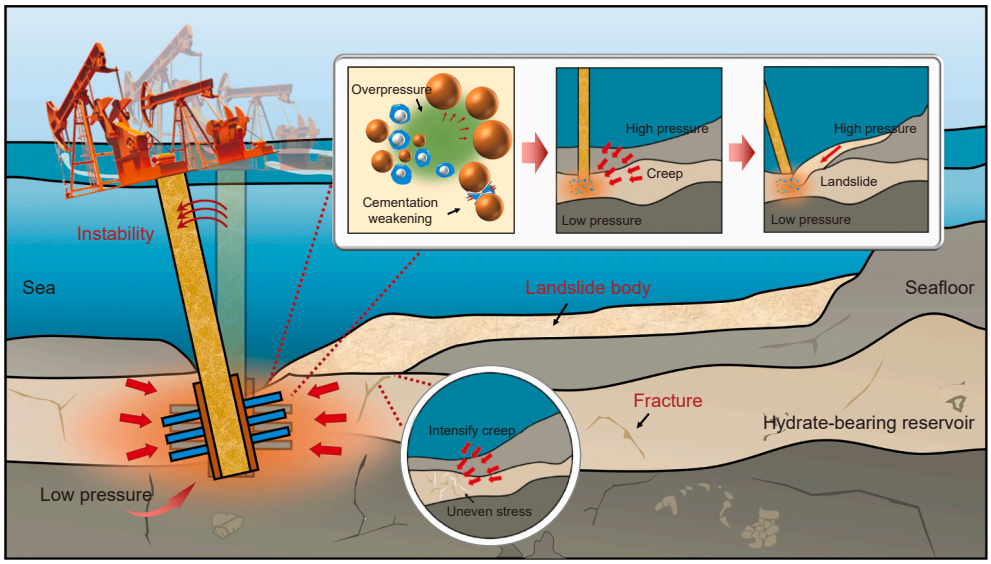


Fig. 1. The role of creep deformation in causing submarine landslides.

Table 1
Fracture distribution in global hydrate reservoirs.

Type	Geographical location	Sediment type	Reference
Land areas	Krishna–Godavari basin in India	Sand and clay	Riedel et al. (2010)
	Ulleung Basin in South Korea	Sand	Lee and Collett (2013)
	Muli basin in China	Siltstone and clayey silt	Peng et al. (2019)
	Coats of Vancouver and Oregon	Sand and clay	Exley et al. (2010)
Marine areas	Qiongdongnan and Taixinan basin in China	Clay	Wei et al. (2021)
	Gulf of Mexico	Sand	Sassen et al. (2001)
	Umitaka spur in the Sea of Japan	Clay	Hiruta and Matsumoto (2022)

during the NGH extraction process. Previous studies have compared the strength and permeability properties of FFHBSs and FHBSs through triaxial experiments. The results indicate that the strength of FFHBSs is typically greater than that of FHBSs. At the same time, it is concluded that the existence of fractures leads to a change in the lag of the permeability fracture point relative to the stress fracture point, which is alleviated with the increase of HS, and the permeability is most sensitive to the strain change in the early stage of shear (Zhang et al., 2024b). Furthermore, in the presence of hydrates, FHBSs exhibit lower cohesion but a larger internal friction angle (Wang et al., 2025b). However, current research into the mechanical properties of FHBSs remains inadequate, particularly regarding their creep properties, which are still not well understood.

Therefore, this study investigates the creep properties of FHBSs using a high-pressure, temperature-controlled hydrate triaxial apparatus, with a comparative analysis performed on FFHBSs. By analysing key parameters such as total creep strain and creep rate, the creep behaviours of both FHBSs and FFHBSs will be elucidated. This research seeks not only to improve the understanding of the creep properties of FHBSs but also to provide theoretical guidance for the engineering geological safety assessment required for the safe extraction of NGHs.

2. Experimental method

2.1. Experimental system

Fig. 2 illustrates the experimental system used in this study. This system has been employed in our previous research (Wang et al., 2025b; Zhang et al., 2024b). This system comprises a gas pressure control unit, a hydrate formation and triaxial mechanics unit, and a data acquisition unit. The in-situ generation and decomposition of methane hydrate, as well as the consolidation, shear, and creep tests of the specimen, can be conducted using this system.

Methane and nitrogen gases were supplied by Jining Xieli Special Gas Co. and Qinhuangdao Aoshen Gas Co., respectively. The ISCO D260 pump, which has a volume of 266.05 mL, was used to generate pore pressures up to 517.1 bar with an accuracy of 0.5%. The temperature was controlled by a TMS8035-R40 thermostatic water bath with a control range of −20 to 50 °C and an accuracy of ±0.1 °C. An LF-50 kN triaxial tester, equipped with a 50 kN maximum axial load (accuracy: ±0.05 kN) and a 100 mm maximum stroke (accuracy: ±0.125 mm), ensured precise measurements. The pressure chamber, fabricated from 316 L stainless steel, can withstand pressures exceeding 16 MPa.

2.2. Specimen preparation

A mixture of montmorillonite and standard sand was used to prepare specimens for this study. Fig. 3 shows the particle size distribution curves for the two materials, along with key grain size parameters (effective grain size d_{10}, median grain size d_{50}, and constraining grain size d_{60}) and the calculated coefficients of curvature (C_c) and uniformity (C_u) (Wang et al., 2020; Zhou et al., 2021). The montmorillonite exhibits $C_u > 5$ and $1 < C_c < 3$, indicating a well-graded particle size distribution. In contrast, the standard sand shows $C_u < 5$ with $C_c < 1$, which corresponds to a poorly-graded particle size distribution (ASTM, 2017).

Consistent with previous studies, the sediment material was prepared by fully mixing montmorillonite and standard sand at a

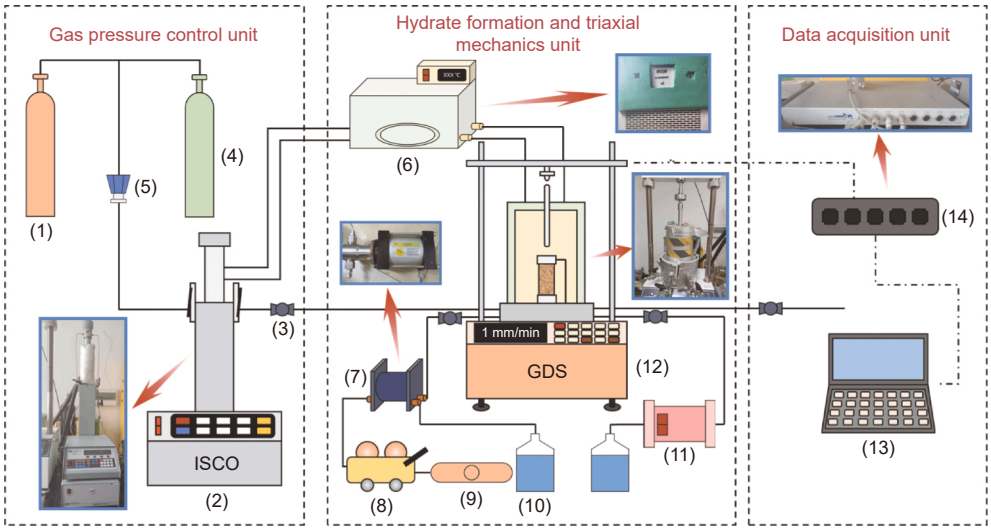


Fig. 2. Schematic of the methane hydrate triaxial test system, with photographs of key devices highlighted by blue rectangles.

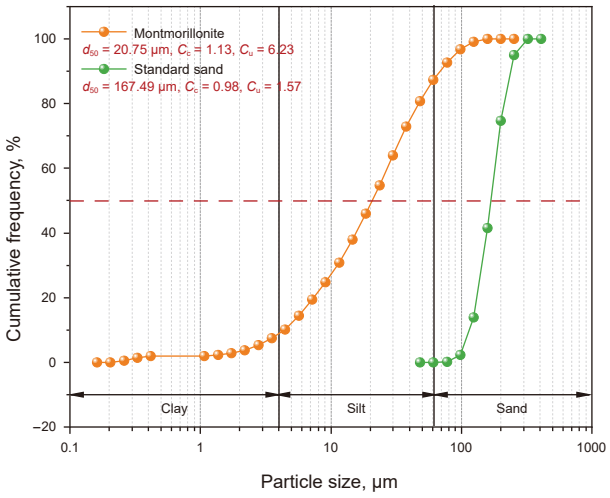


Fig. 3. Particle size distribution.

mass ratio of 1:19, with the mass of montmorillonite being 17.88 g per specimen (Wang et al., 2025b; Zhao et al., 2022; Zhang et al., 2024b). The specific preparation procedure for the fractured specimens was as follows:

(1) Mixing and shaping: The mixture was divided into six equal portions, which were then placed into a cylindrical mould (100 mm in height and 50 mm in diameter). Each portion was compacted by being struck three times with a gravity hammer. At this point, the porosity of the sample is 0.3.

(2) Fracture creation: The shaped specimen was placed into a fracture manufacturing mould. A saw blade was then repeatedly passed through guides in the mould to create the fractures. Ultimately, three fractures with angles of 15°, 45°, and 75° were formed in the upper, middle, and lower positions of the specimen, respectively. Each fracture was rectangular, measuring 20 mm in length and 2 mm in width. To ensure the repeatability and consistency of each experiment, during the process of creating fractures, the penetration angle of the saw blade and the amplitude of repeated pulling are restricted. Then, a sufficient number of sawing operations are carried out to ensure that the cut surface is relatively flat. This range of fracture angles is intended to represent the variability observed in natural hydrate reservoirs, where angles vary with depth and region. For instance, in the shallow section of Hole 10B in the Krishna-Godavari Basin of India, low- and high-angle fractures are present in the deep and shallow layers, respectively (Lee and Collett, 2009). Simultaneously, high-angle fractures are predominant in the shallow section of Hole 5A (Cook and Goldberg, 2008). For the length and width of the fractures, we mainly selected fractures of fixed length and width based on the research of Du et al. (2020), to better study the influence of the existence of fractures on the creep characteristics of hydrate-bearing sediments. This approach is consistent with our previous research (Wang et al., 2020; Zhang et al., 2024b).

(3) Freezing: The prepared specimen was frozen for 12 h to set its structure and ensure its integrity prior to testing.

The preparation procedure for a fractured specimen is illustrated in Fig. 4.

2.3. Experimental process

(1) In-situ NGH formation: The procedure for forming hydrates within the specimen is illustrated in Fig. 5. First, the prepared specimen was removed from the freezer and positioned between the upper and lower platens inside the pressure vessel. Gas and water drainage were facilitated by vents located at the centres of both platens. Second, the specimen was sealed within a 1 mm-thick rubber membrane to prevent contact with the silicone oil used as the confining fluid (confining pressure, CP σ_c). Third, an oil pump and an ISCO pump were used to inject silicone oil into the pressure vessel and methane gas into the pore space of the specimen, respectively. Subsequently, a stepwise method was used to raise both the CP and the pore pressure to 5 MPa (Li et al., 2023a). Throughout this process, the CP was maintained at a pressure slightly higher than the pore pressure to ensure the rubber membrane remained in close

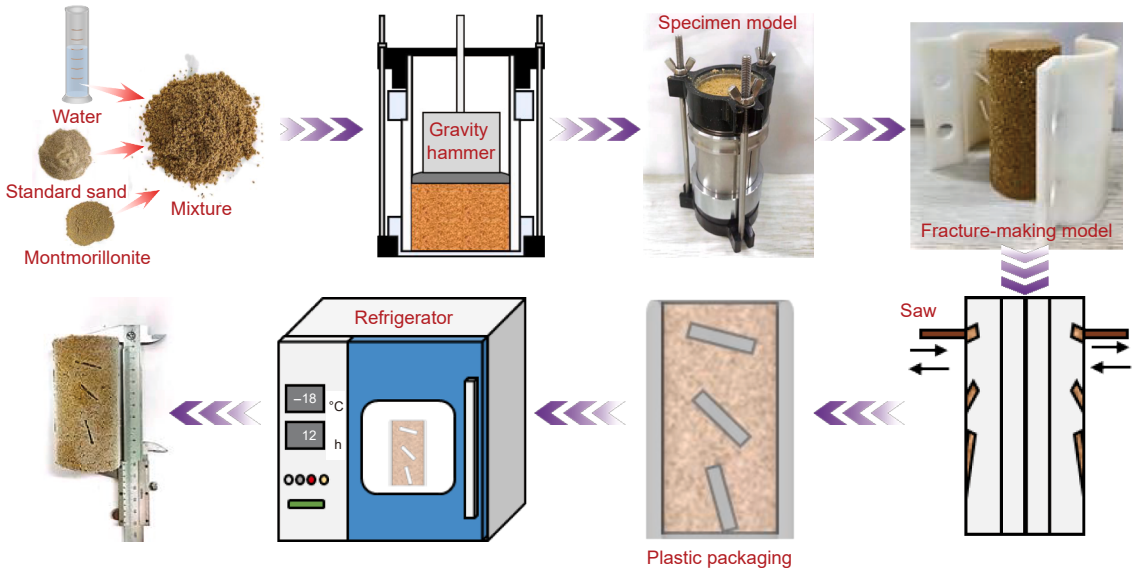


Fig. 4. The specimen preparation process.

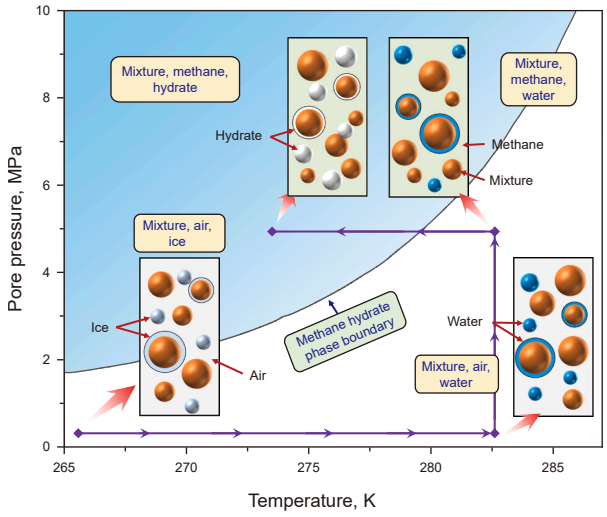


Fig. 5. Hydrate formation process.

contact with the specimen. Finally, the temperature of the thermostatic water bath was set to 0.5 °C. Based on the in-situ temperature and pore pressure conditions of the seabed reservoir and the stability phase diagram of the hydrate, establishing the required pressure and temperature conditions for NGH formation (Zhao et al., 2025). The hydrate saturation measurement method in this study refers to the research of Dong et al. (2020), Li et al. (2023a), Liu et al. (2023c) and Zhao et al. (2022), once gas consumption ceased, the final hydrate saturation was calculated by inputting the volume of methane gas consumed (as measured by the ISCO pump) into Eq. (1) (Wu et al., 2022):

$$S_h = \frac{V_h}{V_p} = \frac{m_h}{\rho_h \cdot V_p} = \frac{\frac{V_m \cdot P_c}{ZRT} \cdot M_h}{\rho_h \cdot V_p} \quad (1)$$

where S_h represents the saturation of NGHs, V_h is the volume of NGHs (mL), V_p denotes the volume of pores within the specimen (mL), m_h represents the mass of NGHs (g), ρ_h is the density of NGHs (g/mL), V_m denotes the volume of consumed methane (mL), P_c represents the pore pressure (MPa), Z is the compressibility factor of methane, R denotes the universal gas constant, T represents the system temperature (K) and M_h is the molar mass of NGHs (g/mol).

(2) Consolidation: Following hydrate formation, a pneumatic-hydraulic booster pump was used to inject silicone oil into the pressure vessel to increase the CP. The specimen was then consolidated for 24 h under a specific effective confining pressure ECP σ'. This duration was sufficient for the ECP-induced sediment deformation to stabilise. The relationship between ECP and CP is given in Eq. (2).

$$\sigma' = \sigma_c - P_c \quad (2)$$

(3) Triaxial creep: After consolidation, the specimen was first subjected to a shear rate of 0.1 %/min until the axial stress reached the desired constant load q_c. Since the vast majority of water in the specimen has been converted into NGHs, this process is an undrained shear. Subsequently, an axial creep test was performed on the specimen under this constant load for a duration of 72 h (Cameron et al., 1990; Chen et al., 2023; Hu et al., 2023; Sun et al., 2024). The constant load was calculated based on the failure strength q_f and the stress ratio R_c, as shown in Eq. (3):

$$q_c = q_f \cdot R_c \quad (3)$$

The failure strength values were determined from our previous studies (Wang et al., 2025b), while the stress ratio R_c was selected based on existing creep studies of HBSs (Chen et al., 2023; Wang et al., 2024; Zhu et al., 2020). The detailed test conditions are provided in Table 2.

3. Results and discussion

3.1. Creep properties of FHBSs

Fig. 6 shows a typical creep curve (secondary consolidation), illustrating the evolution of axial strain in HBSs over time. Based on the creep rate, this process is typically categorised into three

Table 2
Conditions for the triaxial consolidation and creep tests.

Case number	T, K	P_c, MPa	R_c	Specimen type	σ', MPa	S_h, %	q_f, kPa	q_c, kPa
C-1	273.65	5	0.6	Fractured	0.5	0	1217	730.2
C-2						18.66	4016	2409.6
C-3						39.33	4328	2596.8
C-4					1.0	0	2371	1422.6
C-5						19.21	5234	3140.4
C-6						33.52	5262	3157.2
C-7					1.5	0	3328	1996.8
C-8						18.77	5638	3382.8
C-9						38.23	6139	3683.4
C-10				Fracture-free	0.5	0	1241	744.6
C-11						18.51	4430	2658.0
C-12						39.33	5052	3031.2
C-13					1.0	0	2341	1404.6
C-14						19.09	4930	2958.0
C-15						40.48	5686	3411.6
C-16					1.5	0	3513	2107.8
C-17						19.09	5357	3214.2
C-18						33.98	6100	3660.0

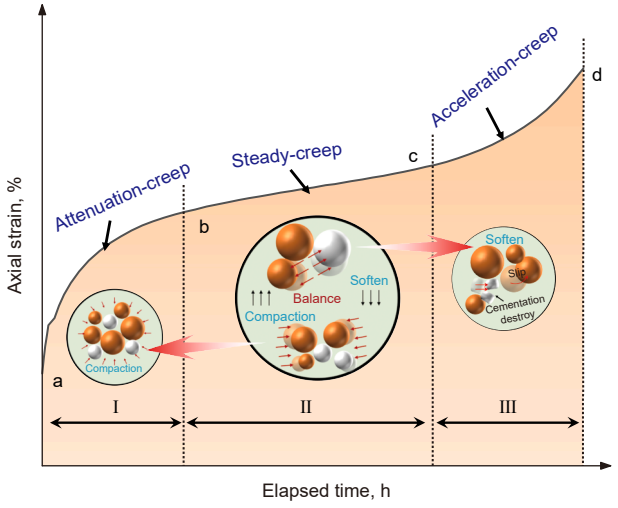


Fig. 6. A typical creep curve illustrating the three distinct stages of creep: attenuation, steady-state, and acceleration.

stages: the attenuation-creep stage, the steady-creep stage, and the acceleration-creep stage. In this study, the starting point of the creep test (point a) is defined as the moment the axial stress reaches the constant load, and the corresponding strain is defined as the initial strain ε_0. The transition from the attenuation-creep stage to the steady-creep stage is marked by the rheological initiation point (point b). Similarly, the transition from the steady-creep stage to the acceleration-creep stage is marked by the damage point (point c) (Li et al., 2024; Wang et al., 2020; Zhu et al., 2020). The attenuation-creep stage is predominantly governed by work-hardening effects and the acceleration-creep stage by softening effects, while the steady-creep stage represents a dynamic equilibrium between the two (Chen et al., 2023; Li et al., 2023c; Wang et al., 2024).

Fig. 7 illustrates the creep curves for FHBSs under various HS. The acceleration-creep stage is only observed in the specimen with no hydrates (S_h = 0%) tested at an ECP of 0.5 MPa. This can be attributed to two combined factors. First, under a relatively low ECP, the specimen is less compacted and therefore exhibits weaker deformation resistance. Second, the absence of hydrates means there is no inter-particle cementation to provide structural

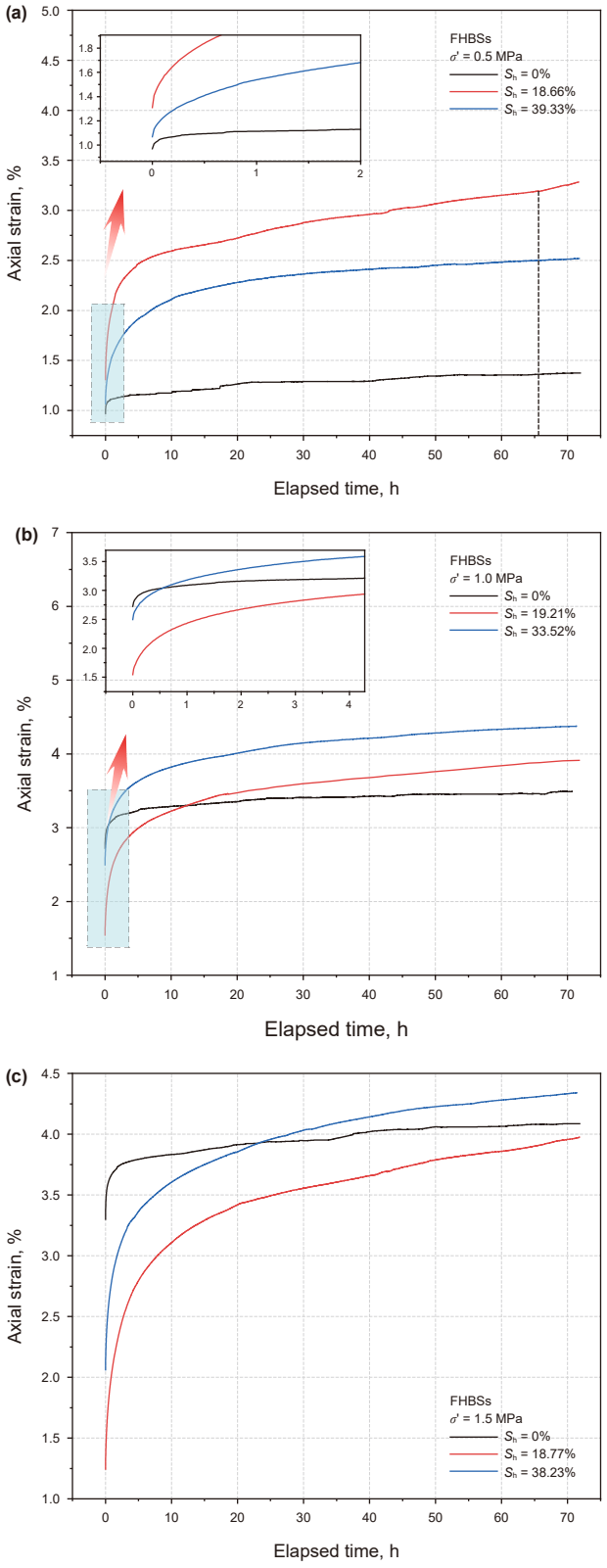


Fig. 7. Creep curves for fractured hydrate-bearing sediments (FHBSs) at various hydrate saturations (S_h) under ECPs (σ') of **(a)** 0.5 MPa; **(b)** 1.0 MPa; **(c)** 1.5 MPa.

support. Consequently, the uncemented sediment is more prone to structural failure under sustained loading, leading to the onset of the acceleration-creep stage. The general absence of this stage in

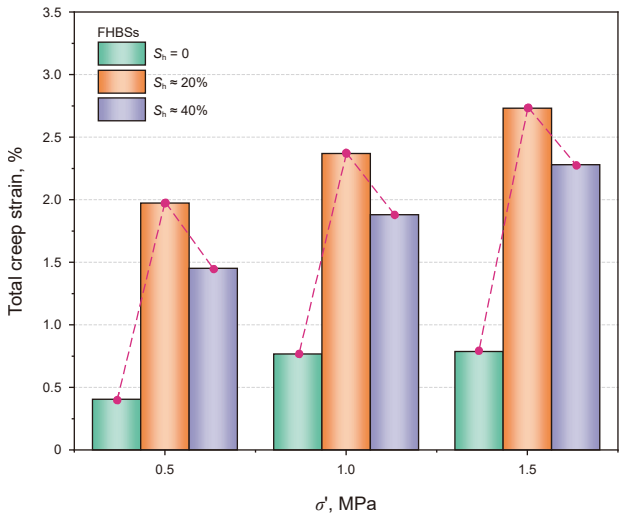


Fig. 8. TCS of FHBSs as a function of S_h under different ECPs.

the other tests is consistent with the results of similar triaxial creep experiments conducted by other researchers on HBSs (Li et al., 2016; Nakashima et al., 2021). It should also be noted that the initial strain ε_0 depends on the stress-strain response during the initial shearing phase required to reach the target creep stress. As this is primarily related to the material's strength properties, a detailed analysis can be found in our previous study (Wang et al., 2025b).

Fig. 8 presents the total creep strain (TCS) of FHBSs during the creep process. As HS increases, the TCS initially rises and then declines. As we previously reported, FHBSs at 20% and 40% HS show comparable failure strengths, which exceed those of the 0% saturation specimens (Wang et al., 2025b). Therefore, FHBSs with an HS of 0% are subjected to the minimum constant stress. During the compression process, the friction and extrusion between particles develop more frequently, exhibiting stronger resistance to deformation. In FHBSs with 20% HS, hydrates predominantly accumulate near fractures, leading to a non-uniform stress distribution within the specimen and facilitating particle rotation and slippage (Wang et al., 2025b). Moreover, the lower HS results in thin and brittle hydrate deposits at fractures within the FHBSs. Compared to the well-developed cementation network in high-saturation FHBSs, these fragile structures provide weaker support, making the material more prone to deformation under constant loading (Gabitto and Tsouris, 2010). Additionally, hydrates can undergo dynamic dissociation and regeneration under phase equilibrium conditions, which provides favourable conditions for fracture deformation, particularly for FHBSs with relatively low hydrate content (Durham et al., 2003; Sun et al., 2023). In summary, the parameter evolution observed in FHBSs during creep results from multi-field coupling, as shown in Fig. 9.

Furthermore, as the ECP increases, the TCS is observed to rise. An increase in ECP exerts a compaction effect on the specimen, which intensifies friction between particles and thereby enhances the intrinsic deformation resistance of the FHBSs (Wang et al., 2023; Xu et al., 2023). However, under the experimental conditions of this study, a higher ECP is accompanied by a higher constant creep load. This increase in the applied stress is the dominant factor, ultimately leading to a greater TCS.

Based on the total creep behaviour shown in Fig. 8, the creep strain during the attenuation-creep stage (Fig. 10), the creep rate during the attenuating-creep stage (Fig. 11), and the rate during the steady-creep stage (Fig. 12) were statistically analysed. The relationships between these three parameters and HS under various ECPs are consistent with the trend observed for the TCS. This implies that under the corresponding constant loads, the deformation resistance of the FHBSs ranks in the following order of hydrate saturation: 0% > 40% > 20%.

In addition, as the ECP increases, the attenuation-creep rates (ACR) for the experimental groups with HS of 20% and 40% are

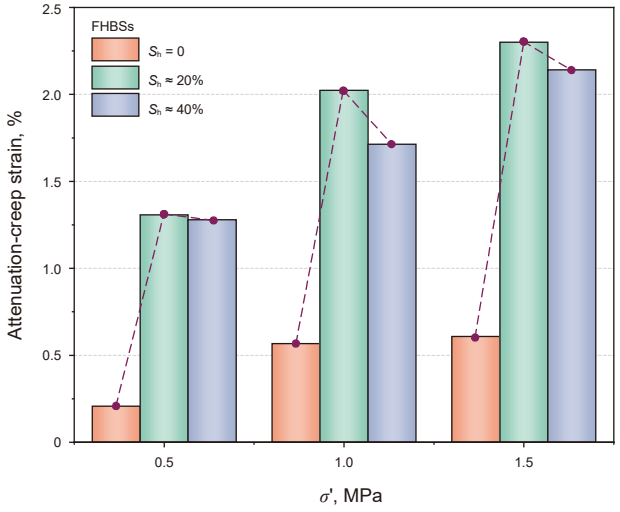


Fig. 10. ACS of FHBSs as a function of S_h under various ECPs.

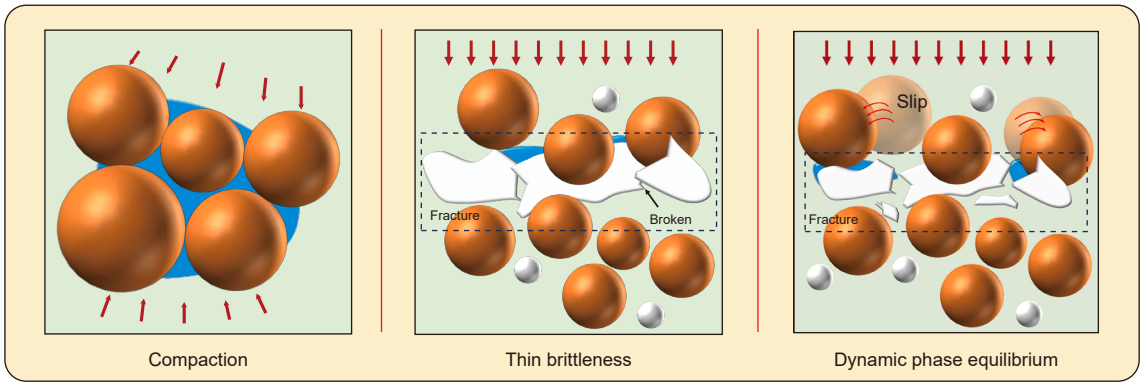


Fig. 9. The microscopic change mechanism in FHBSs during the creep process.

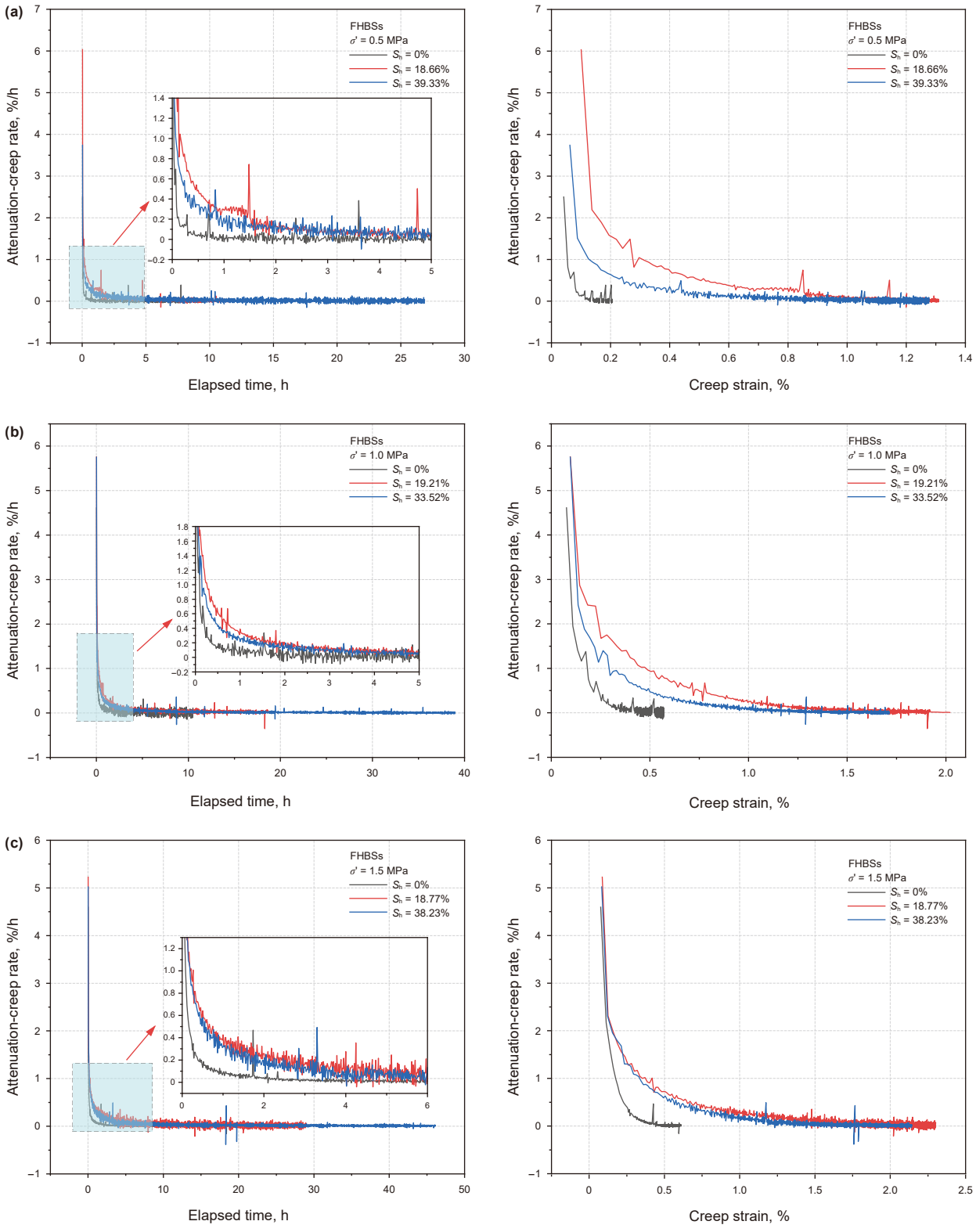


Fig. 11. ACR for FHBSs at various S_h under ECPs of **(a)** 0.5 MPa; **(b)** 1.0 MPa; **(c)** 1.5 MPa.

observed to converge. This can be explained by the differing responses of the specimens to compaction. For the FHBS with 20% HS, an increase in ECP leads to fracture closure and specimen compaction. This brings hydrate particles into closer contact with sand particles, densifying the initially weak cementation network and thereby enhancing the specimen's deformation resistance (Wei et al., 2023). In contrast, for the FHBSs with 40% HS, the hydrates are already more compactly distributed. Consequently, the compaction effect from the increased ECP is less pronounced, resulting in only a slight improvement in its resistance to

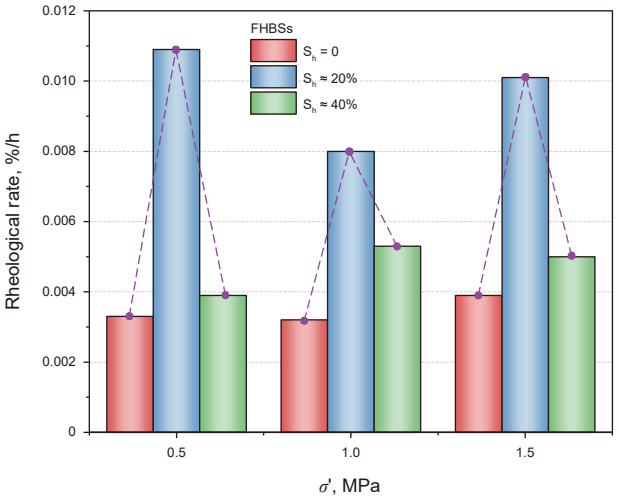


Fig. 12. RR of FHBSs as a function of S_h under various ECPs.

deformation. This result indicates that the sensitivity of the deformation resistance of FHBSs to ECP decreases as the ECP increases, particularly under high HS conditions (Liu et al., 2023a). This behaviour can be attributed to the coupled effects of particle compaction (a hardening mechanism) and potential damage to the hydrate's cementation structure under high pressures (a softening mechanism). The initial HS dictates the internal structure of the FHBSs, which in turn governs how their creep behaviour responds to these competing effects under increasing ECP.

As the ECP increases, it is also noted that the attenuation-creep strain (ACS) follows the same variation trend as the TCS, while the rheological rate (RR) behaves differently. This suggests that the key structural rearrangement processes, such as initial particle rearrangement, cementation damage, and fracture closure, occur predominantly during the attenuation-creep stage rather than the steady-creep stage. Consequently, the ACS plays a more significant role in determining the final TCS.

Fig. 13 illustrates the rheological initial time (RIT) of the FHBSs under different saturations. As the RIT, which represents the duration of the attenuation-creep stage, is observed to increase with rising HS. This trend can be attributed to the following factors: (1) At HS = 0%: In the absence of any hydrate cementation, the sediment particles can rearrange rapidly in response to the applied stress, resulting in the shortest RIT and the earliest onset of the steady-creep stage. (2) At HS = 20%: The specimen contains a partial and likely brittle cementation network. This structure provides some initial resistance but is susceptible to damage under constant loading, prolonging the time required to reach a steady state compared to the hydrate-free case (Chuvilin et al., 2018). (3) At HS = 40%: The presence of a denser hydrate network provides significant structural integrity. Consequently, the processes of breaking these more robust cementation bonds and rearranging the particles require more time to complete, leading to the longest observed RIT (Zhou et al., 2024).

Additionally, the RIT is observed to increase with increasing ECP. This is because the higher ECP enhances inter-particle friction and compaction. This increased resistance to particle rearrangement results in a slower attainment of the steady-creep stage and thus a longer RIT. This finding is contrary to that of Zhu et al. (2020), who reported a decrease in RIT with increasing ECP. The discrepancy can likely be attributed to fundamental differences in both hydrate morphology and the host sediment used (Wu et al., 2022). In the present study, hydrates were generated *in situ* and formed cementing structures within the fractures and between particles. In contrast, the research conducted by Zhu et al. (2020) involved preparing samples by mixing hydrates with quartz sand particles. This resulted in the hydrates in the samples being in the form of pore-filling hydrates, and these hydrates provided much weaker structural cohesion and resistance to deformation. In this study, the existence of fractures in the samples led to the hydrate mainly existing in a cemented structure. This sample preparation method is fundamentally different from Zhu et al. (2020). The role played by the cemented structure when the samples is subjected to force enables the samples to exhibit stronger structural cohesion and resistance to deformation. Furthermore, the sediment matrix itself plays a crucial role. Zhu et al. (2020) used kaolinite, which has distinct chemo-mechanical properties compared to the sand-montmorillonite mixture used here. In their kaolinite specimens, an increase in ECP reportedly promoted several softening mechanisms, including particle fragmentation and the melting of any co-existing ice (due to freezing point depression). These processes could lead to water-induced swelling of the kaolinite and accelerate hydrate decomposition, both of which would cause the specimen to deform more easily and shorten the RIT (Zhu et al.,

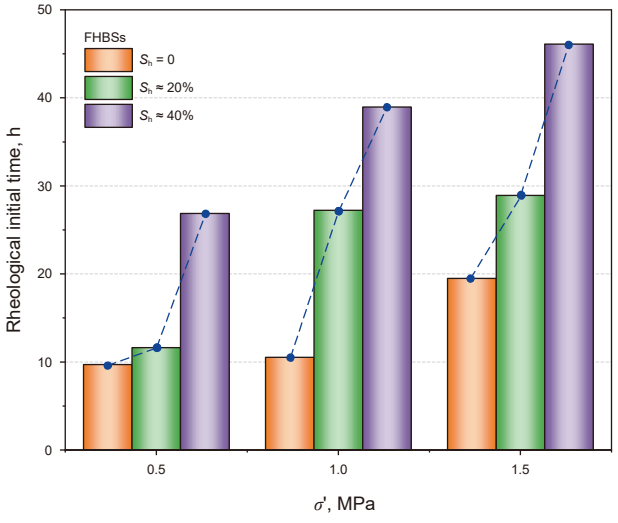


Fig. 13. Rheological initial time for FHBSs as a function of S_h under various ECPs.

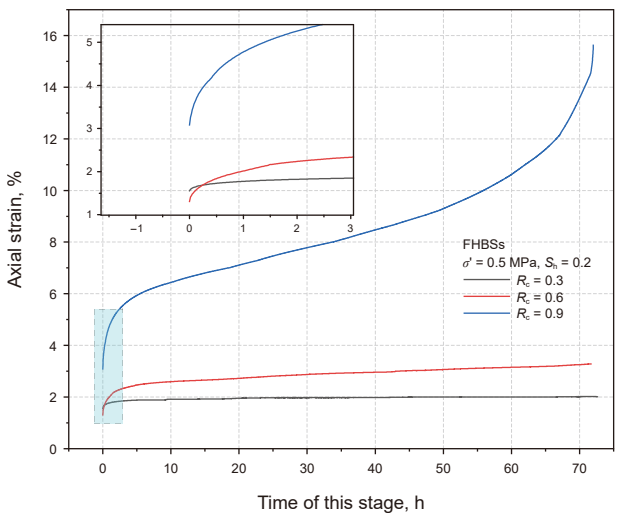


Fig. 14. Creep curves of FHBSs with different R_c at an ECP of 0.5 MPa and S_h of 20%.

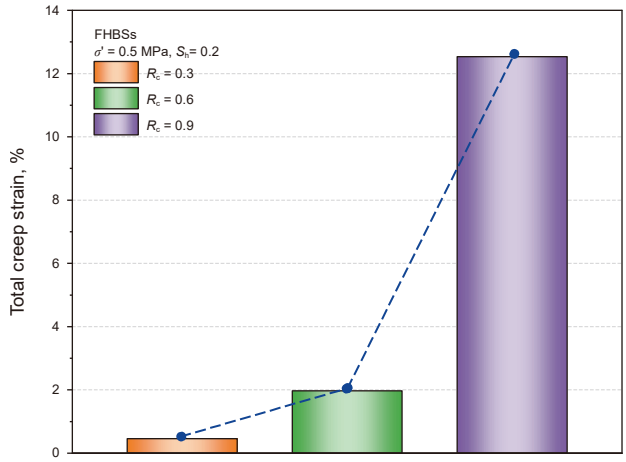


Fig. 15. TCS of FHBSs with different R_c at an ECP of 0.5 MPa and S_h of 20%.

2020). It should be emphasized here that the swelling ability of kaolinite upon contact with water is much higher than that of the mixture of montmorillonite and quartz sand in this paper (Radjai et al., 1998). In summary, the distribution properties of hydrates greatly determine the deformation resistance of FHBSs.

In addition, we also studied the creep curves of FHBSs with an ECP of 0.5 MPa and a hydrate saturation of 20% under different creep stress ratios, as shown in Fig. 14. The results demonstrate that only when R_c attains a value of 0.9 the samples manifest an evident accelerated creep stage. This phenomenon can be ascribed to the fact that a higher R_c entails a greater continuous load. Under such condition, the FHBSs become more susceptible to structural failure, which in turn triggers the onset of the accelerated creep stage. As can be observed from Fig. 15, the TCS of FHBSs during the creep process exhibits a continuous increase with the elevation of R_c, which is consistent with the research on the creep deformation of hydrate-bearing frozen clay at different creep stress ratios prepared by the "mixture method" (Zhu et al., 2020). The underlying mechanism is that as R_c increases and the continuous load is applied, the hydrate cementation structure within the samples is more likely to fracture. This promotes the propagation of fractures and intensifies structural damage, ultimately leading to greater creep deformation (Liu et al., 2023b; Yang et al., 2010).

Fig. 16(a) and (b) further analysed the strain and its rate during the attenuation-creep strain stage. It was discovered that the ACS exhibited a similar variation trend to the TCS under different R_c

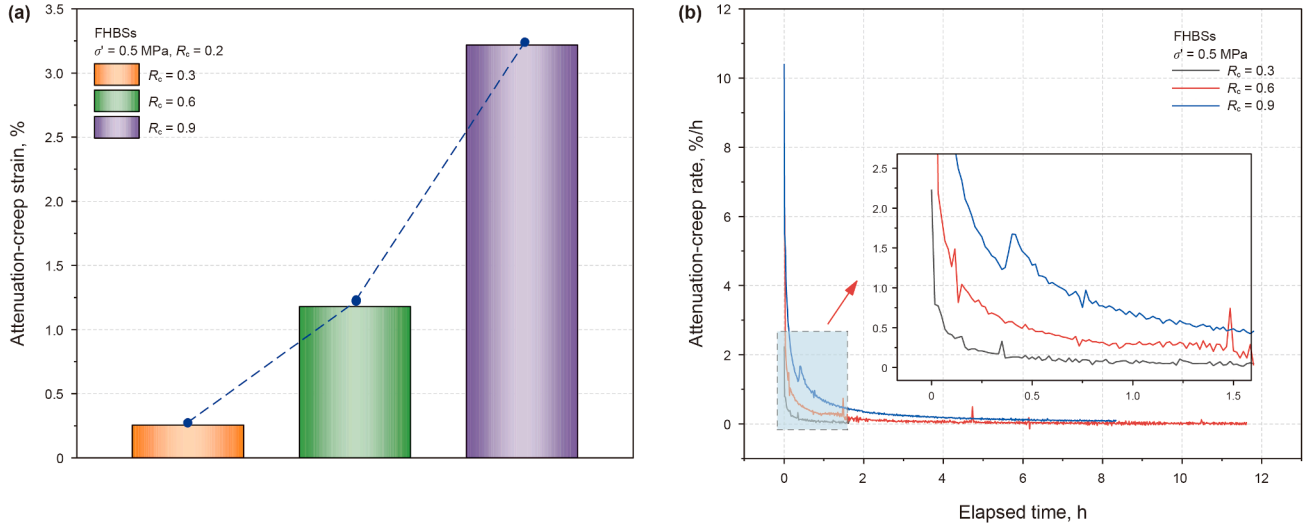


Fig. 16. Parameters of the attenuation creep stage of FHBSs with different R_c at an ECP of 0.5 MPa and S_h of 20%: **(a)** ACS; **(b)** ACR.

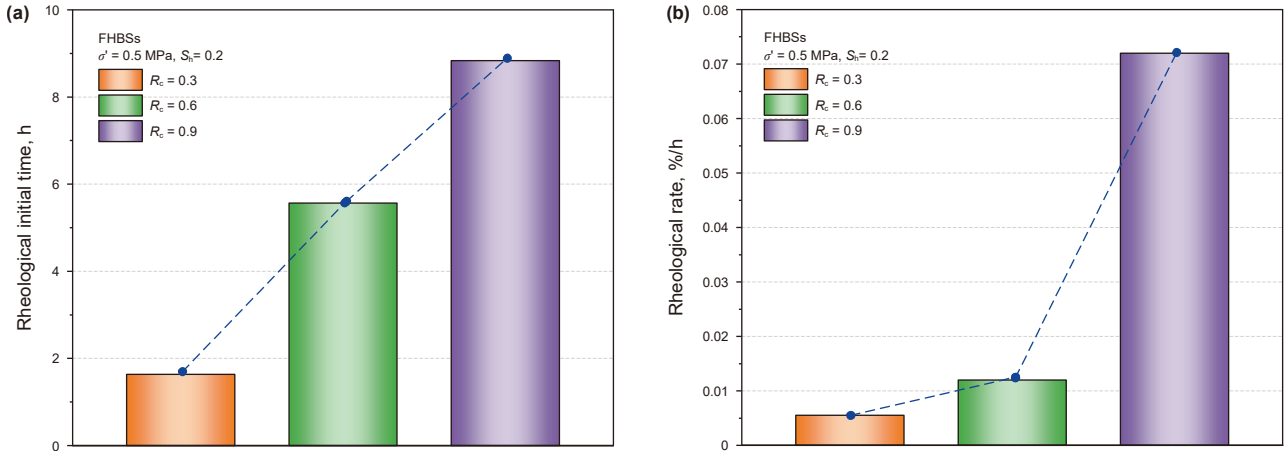


Fig. 17. Rheological parameters of FHBSs with different R_c at an ECP of 0.5 MPa and S_h of 20%: **(a)** RIT; **(b)** RR.

conditions. This finding implies that R_c exerts a significant influence on the creep characteristics of FHBSs. Regarding the ACS, when compared with samples at a low stress ratio, samples at a high stress ratio demonstrate a slightly elevated strain rate. Although the strain rate of samples with a high R_c at the same time point is marginally higher than that of samples with a low R_c, the overall difference is not substantial.

As shown in Fig. 17(a), the RIT of FHBSs under different R_c conditions increase with the increase of R_c. This is mainly because a higher R_c leads to an increase in continuous load, thereby enhancing the friction and compressive effect between particles, hindering the re-arrangement of particles, and thus delaying the time to enter the steady-creep stage, resulting in a corresponding increase in RIT. Fig. 17(b) shows that the RR increases with the increase of R_c, especially when R_c reaches 0.9, its rate increases significantly. This is because the particles inside the sample have been rearranged closely during the attenuation-creep stage. When reaching the steady-creep stage, the creep variable and rate are mainly affected by the continuous load.

3.2. Creep properties of FFHBSs

For comparison, the creep properties of FFHBSs were also investigated. Fig. 18 illustrates the creep curves for FFHBSs at different HS, showing that none of the specimens reached the acceleration-creep stage within the 72-h test duration. The TCS

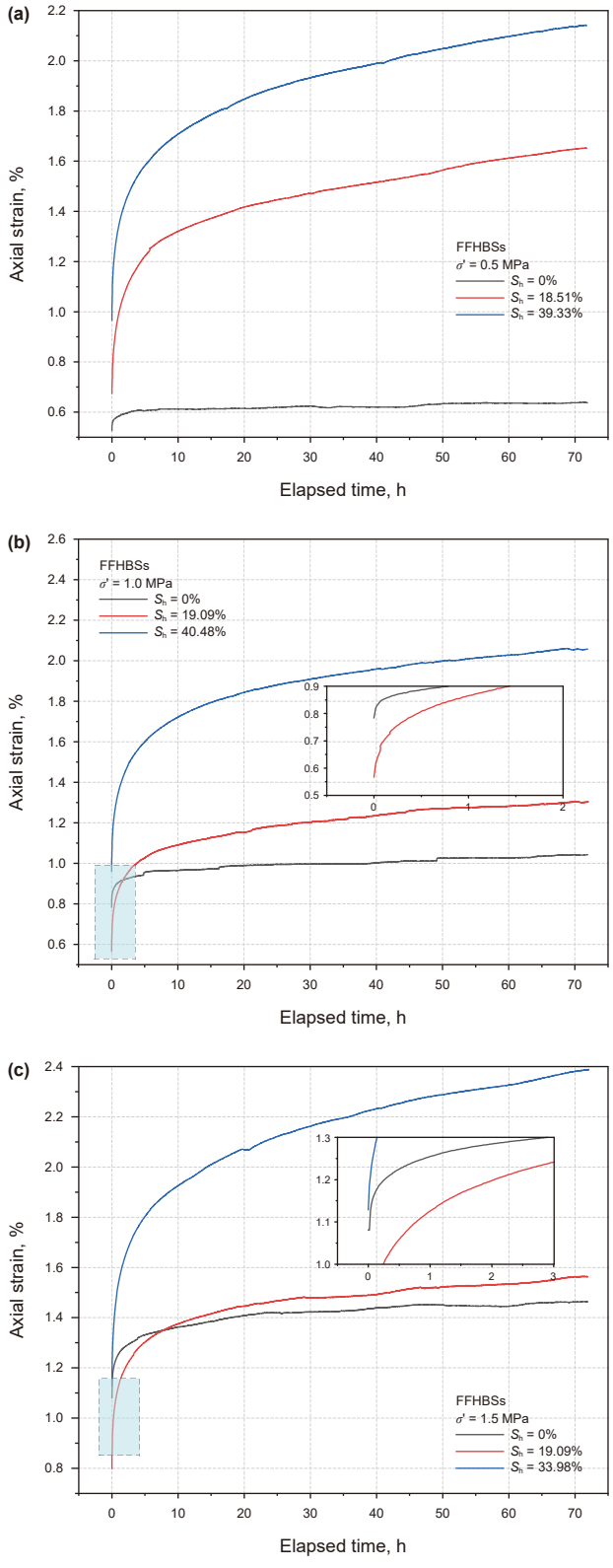


Fig. 18. Creep curves of FFHBSs at different S_h: **(a)** ECP equals 0.5 MPa; **(b)** ECP equals 1.0 MPa; **(c)** ECP equals 1.5 MPa.

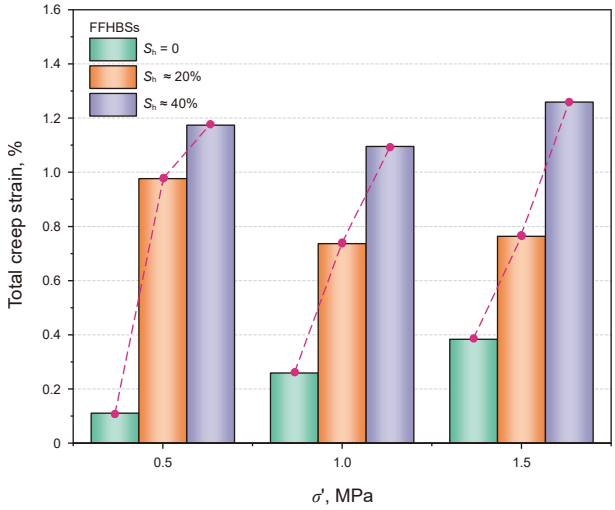


Fig. 19. TCS of FFHBSs as a function of S_h under various ECPs.

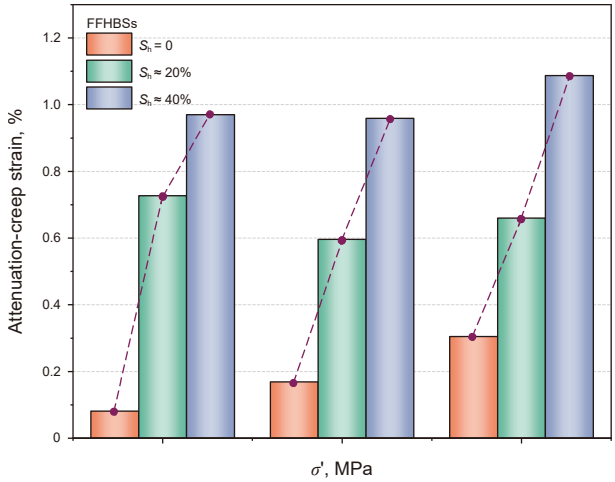


Fig. 20. ACS of FFHBSs as a function of S_h under various ECPs.

was plotted from these curves and is shown in Fig. 19. It is clear that, in contrast to the behaviour of the fractured specimens, the TCS of FFHBSs increases with increasing HS at all tested ECPs. This is primarily because the constant load applied during the creep test, which is based on the failure strength, also increases with HS (Zhang et al., 2024b). While FFHBSs with 40% hydrate saturation exhibit a higher failure strength, this strength is mobilised at large strains (approximately 20%), by which point the specimen has been significantly compacted. In contrast, the creep process occurs at much lower strains where the specimen is less compacted, and deformation is predominantly governed by damage to the hydrate cementation bonds under the applied load (Chen et al., 2023; Liu

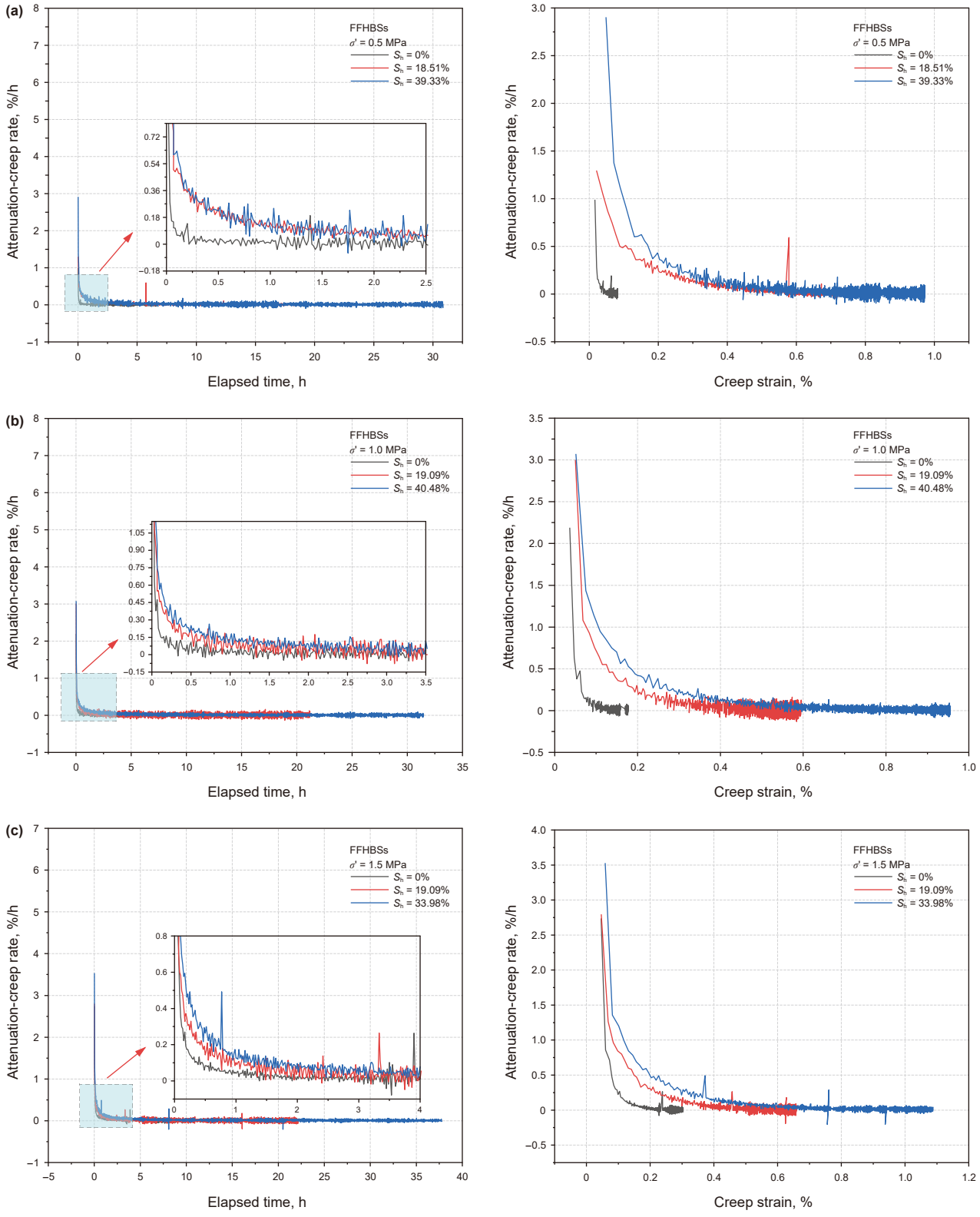


Fig. 21. ACR for FFHBSs at various S_h under ECPs of: **(a)** 0.5 MPa; **(b)** 1.0 MPa; **(c)** 1.5 MPa.

et al., 2024). Therefore, for the FFHBSs, the structural support provided by the increased hydrate content is insufficient to counteract the greater deformation caused by the correspondingly higher constant creep load.

Figs. 20–22 show the ACS, ACR, and RR of the FFHBSs, respectively. For these specimens, the trends for all three parameters follow that of the TCS, increasing consistently with rising HS. The ACRs for FFHBSs with 20% and 40% HS do not converge with increasing ECP, which is a distinct contrast to the behaviour observed in the FHBSs. This finding validates the explanation provided in Section 3.1, which attributed the convergence phenomenon specifically to fracture-related mechanisms. The absence of this behaviour in the fracture-free specimens strongly suggests that fractures fundamentally alter the occurrence state of hydrates within the sediment, whereas in FFHBSs, the hydrate particles are distributed more uniformly throughout the sediment matrix.

A pattern similar to that of the FHBSs is also observed in the FFHBSs: the attenuation-creep strain (ACS) varies with ECP in the same manner as TCS, whereas RR does not. This consistency across both specimen types suggests that the TCS is predominantly governed by the ACS, irrespective of the presence of fractures. Furthermore, for all hydrate-bearing specimens, the ACS shows limited sensitivity to changes in ECP, an observation that aligns with the results of Zhu et al. (2020). Finally, when comparing the

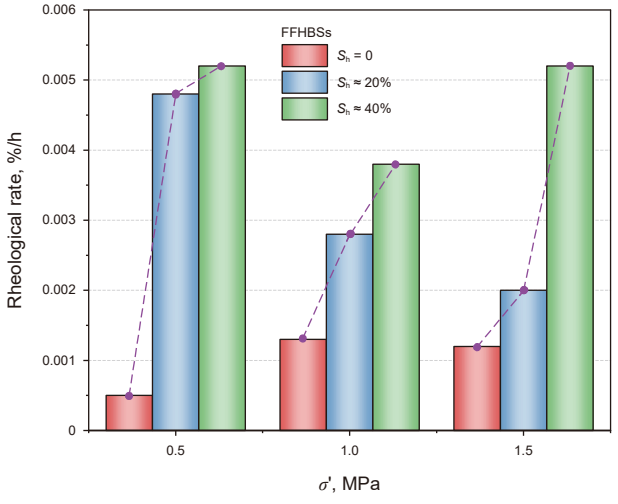


Fig. 22. RR of FFHBSs as a function of S_h under various ECPs.

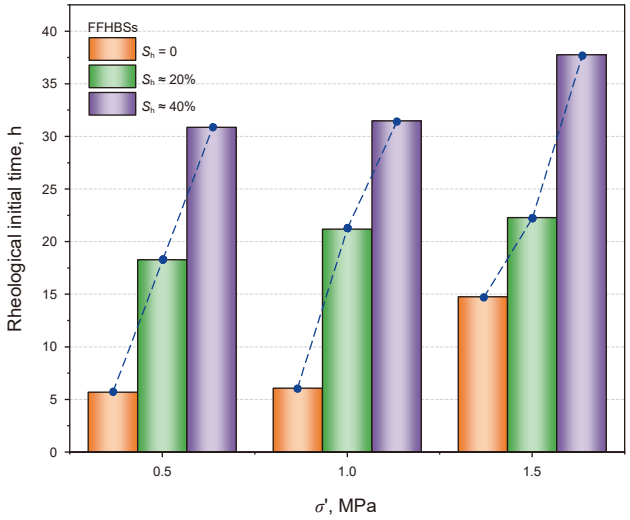


Fig. 23. Rheological initial time of FFHBSs at different S_h.

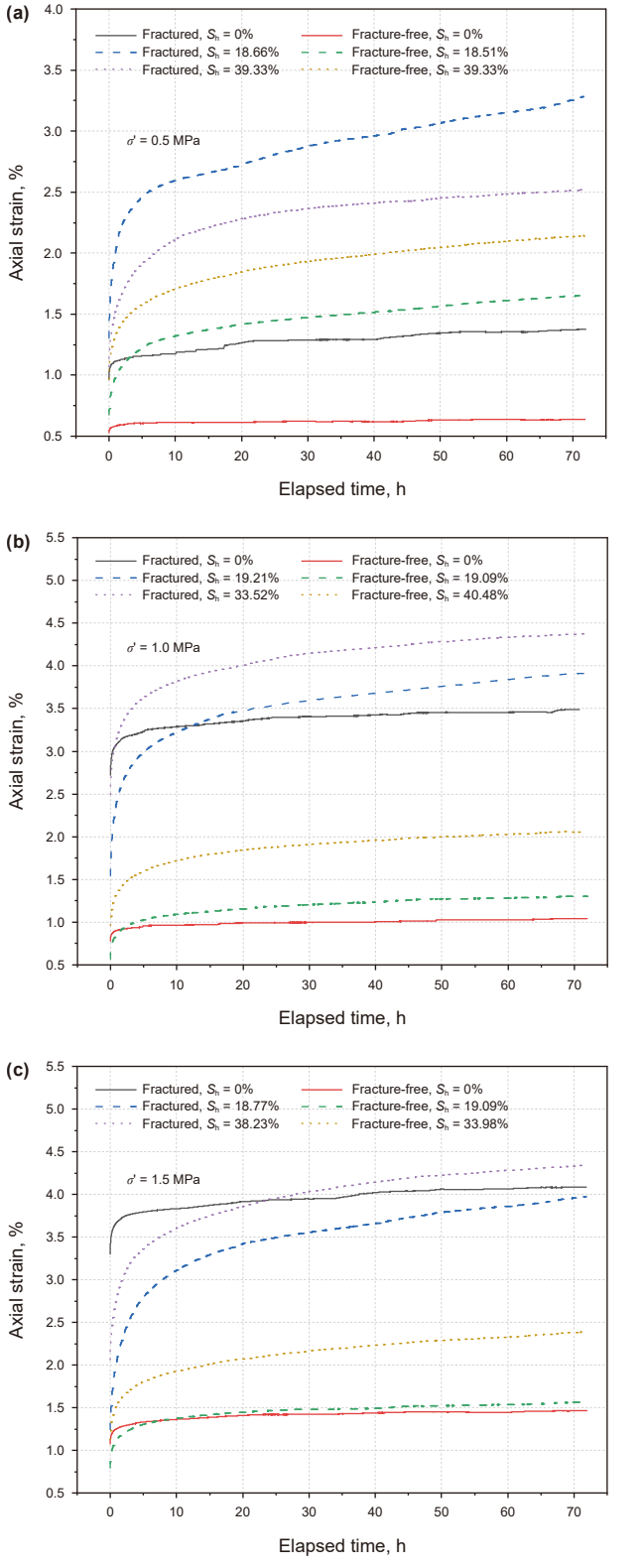


Fig. 24. Comparison of creep curves between FFHBSs and FHBSs: **(a)** $\sigma' = 0.5$ MPa; **(b)** $\sigma' = 1.0$ MPa; **(c)** $\sigma' = 1.5$ MPa.

influence of the two main experimental variables, a clear conclusion can be drawn. For both FHBSs and FFHBSs, the variations in the measured creep parameters with hydrate saturation exhibit more systematic and predictable trends compared to their variations with ECP. This suggests that, within the experimental conditions of this study, HS is a more dominant factor than ECP in controlling the creep behaviour of these sediments.

Fig. 23 shows the RIT at different saturations for the FFHBSs. The duration of the attenuation-creep stage is observed to be positively correlated with both HS and ECP, displaying the same pattern as that recorded for the FHBSs. This consistent behaviour indicates that the presence of fractures does not alter the fundamental influence of HS and ECP on the RIT.

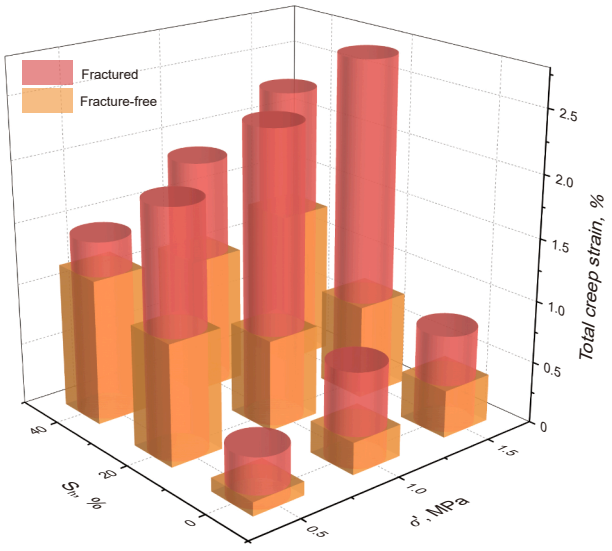


Fig. 25. Comparison of TCS between FHBSs and FFHBSs under various test conditions.

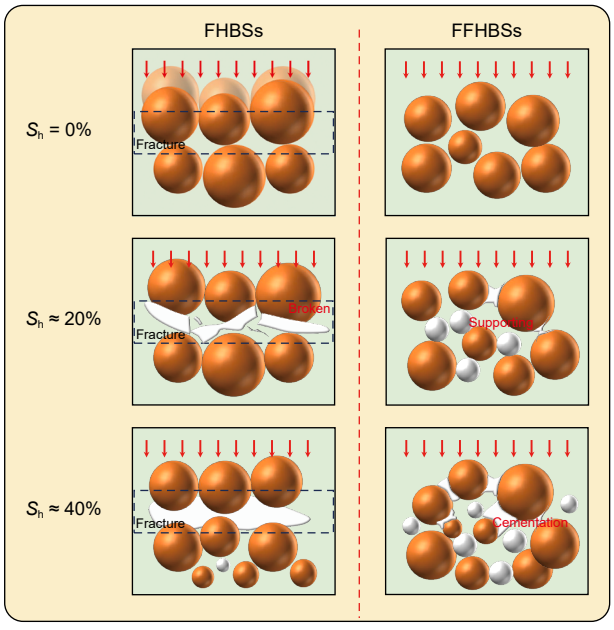


Fig. 26. Schematic diagram illustrating the proposed creep deformation mechanisms in FHBSs versus FFHBSs.

3.3. Comparison of creep properties between FHBSs and FFHBSs

This section provides a direct comparison of the creep properties of FHBSs and FFHBSs. Fig. 24 shows the creep curves for both specimen types under identical test conditions. Based on these data, the TCS, ACS, and RR were determined for a comparative analysis.

As shown in Fig. 25, the TCS of the FHBSs is consistently greater than that of the FFHBSs under all tested conditions of HS and ECP. This difference can be attributed to the influence of the fractures on the sediment structure at varying hydrate saturations: (1) At HS = 0%, the pre-existing fractures in the FHBSs act as planes of weakness that provide additional void space, allowing for greater axial compaction under load compared to the more uniform FFHBSs. (2) At HS = 20%, in the FHBSs, hydrates preferentially form within the fractures, leading to a heterogeneous structure with localised, thin, and brittle cementation that is susceptible to

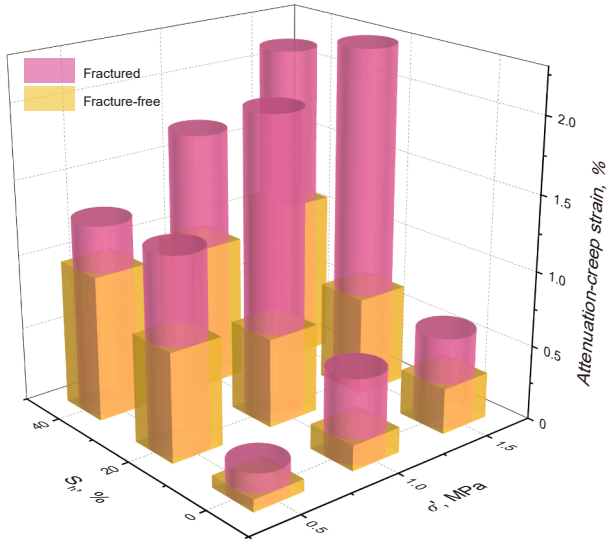


Fig. 27. Comparison of the ACS between FFHBSs and FHBSs under various test conditions.

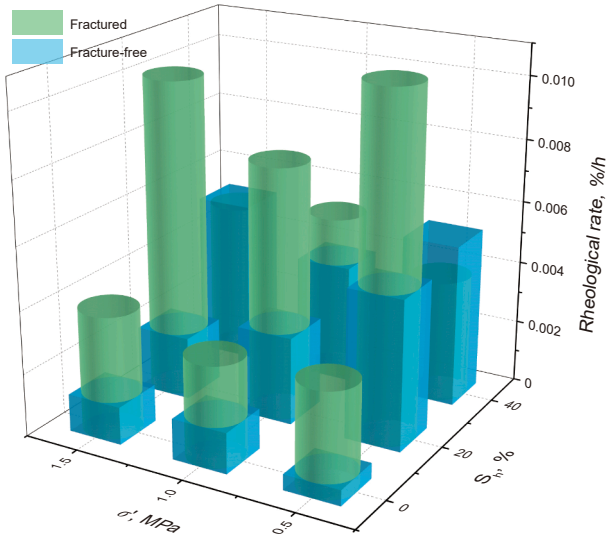


Fig. 28. Comparison of the RR between FFHBSs and FHBSs under various test conditions.

Table 3
Experimental conditions for the additional shear and creep tests.

Case number	T, K	P_c, MPa	R_c	Specimen type	σ', MPa	S_h, %	q_f, kPa	q_c, kPa
S-a	273.65	5	0.6	Fractured	0.5	0	1217	-
S-b						9.83	3735	-
S-c						15.8	3918	-
S-d						22.7	4016	-
S-e						26.8	4321	-
S-f						32.8	4319	-
S-g						37.7	4328	-
C-a						0	-	730.2
C-b						10.10	-	2241
C-c						14.50	-	2350.8
C-d						18.66	-	2409.6
C-e						26.50	-	2592.6
C-f						32.80	-	2591.4
C-g						39.33	-	2596.8

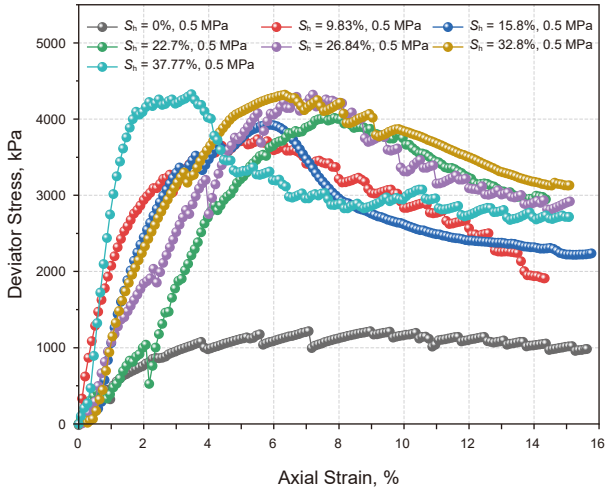


Fig. 29. Deviatoric stress-strain curves for FHBSs at various S_h under an ECP of 0.5 MPa.

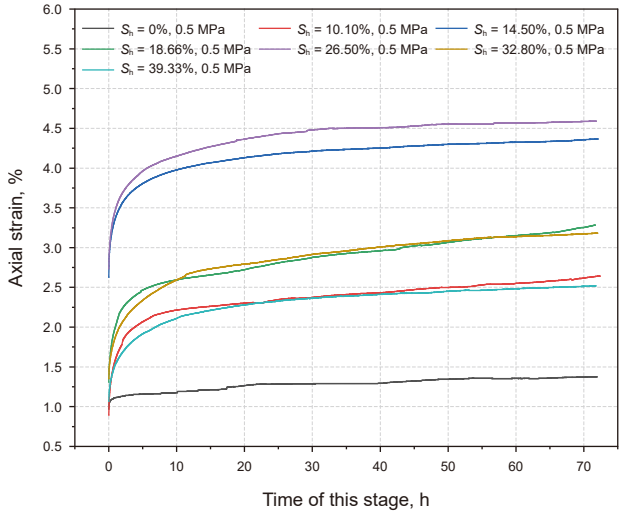


Fig. 30. Creep curves for FHBSs at various S_h under an ECP of 0.5 MPa.

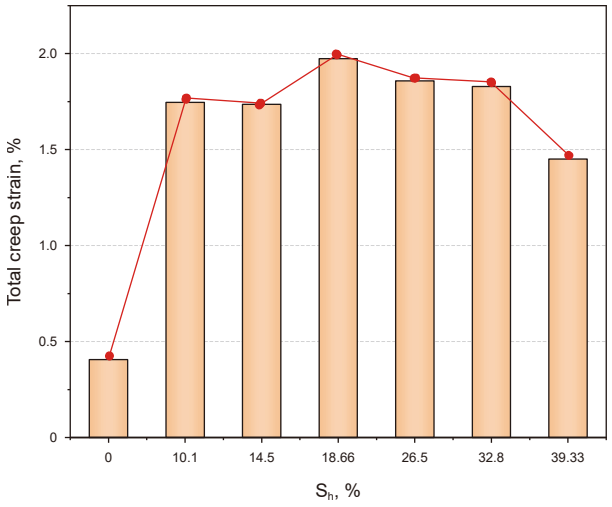


Fig. 31. TCS for FHBSs under an ECP of 0.5 MPa.

breaking during creep. In contrast, the FFHBSs develop a more uniform, interlocking cementation network throughout the sediment matrix, which provides greater overall resistance to deformation (Li et al., 2022). (3) At HS = 40%, even at this higher saturation, where the hydrate network in the FHBSs is denser, the inherent structural discontinuity caused by the fractures persists. The more homogeneous cementation network within the FFHBSs remains structurally superior and therefore more resistant to creep deformation (Wei et al., 2023; Zhang et al., 2011). A schematic illustrating these differing deformation mechanisms is presented in Fig. 26. The fact that the structural differences between the two specimen types are so clearly reflected in the total creep strain reinforces the conclusion from Section 3.1: the defining deformation processes occur predominantly during the attenuation-creep stage.

Figs. 27 and 28 present a comparison of the ACS and RR for both specimen types. As expected, ACS exhibits a phenomenon consistent with the TCS, where the strain in FHBSs is consistently higher. This corresponds to the results discussed in sections 3.1 and 3.2. The following explanations are given for the comparative results of RR: (1) Multiple sets of conditions showed that FHBSs possessed higher RRs, with higher RRs being observed only for FFHBSs with 40% HS and ECPs of 0.5 MPa and 1.5 MPa. This is because the presence of the fracture reduces the deformation resistance of FHBSs as a whole, for the reasons expressed in the previous section. (2) HS is 40%, ECP is 0.5 MPa: An ECP of 0.5 MPa and a constant load of 2596.8 kPa failed to have a damaging effect on the hydrate at the fracture. Fracture-filling hydrates in the rheological stage provide solid support for the FHBSs. As a result, FHBSs have a lower RR relative to FFHBSs. (3) HS is 40%, ECP is 1.5 MPa: The HS of the FHBSs is 4.25% higher than that of FFHBSs, which enriches the backbone network of the FHBSs (Huaimin et al., 2018). The difference in RR between the FHBSs and FFHBSs is only 0.0002 %/h, so it is likely that the FHBSs would have had a higher RR than the FFHBSs without this extra saturation. This suggests that an additional HS of about 4% compensates for the lower resistance to deformation caused by the fracture structure.

3.4. Critical saturation of creep properties of FHBSs

As observed previously, the TCS of FHBSs exhibits a non-monotonic trend, first increasing and then decreasing with rising

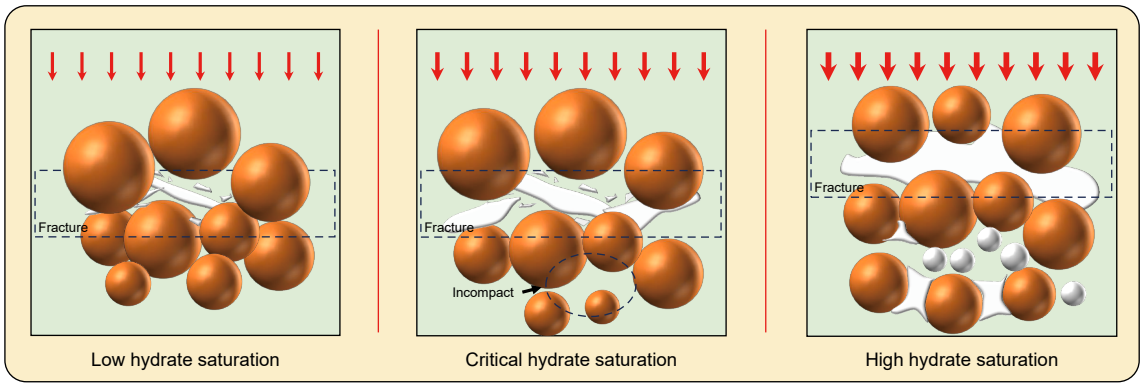


Fig. 32. Schematic diagram illustrating the proposed mechanisms for the creep behaviour of FHBSs at S_h below and above the critical saturation point.

Table 4
Detection of model predictive ability.

Specimen type	S_h, %	σ', MPa	TCS calculated value	TCS experimental value	Error, %	ACS calculated value	ACS experimental value	Error, %
Fractured	14.5	0.5	1.8715	1.7361	7.2	1.3962	1.3699	1.88
	32.8	0.5	1.7778	1.8293	2.9	1.4756	1.3084	11.3

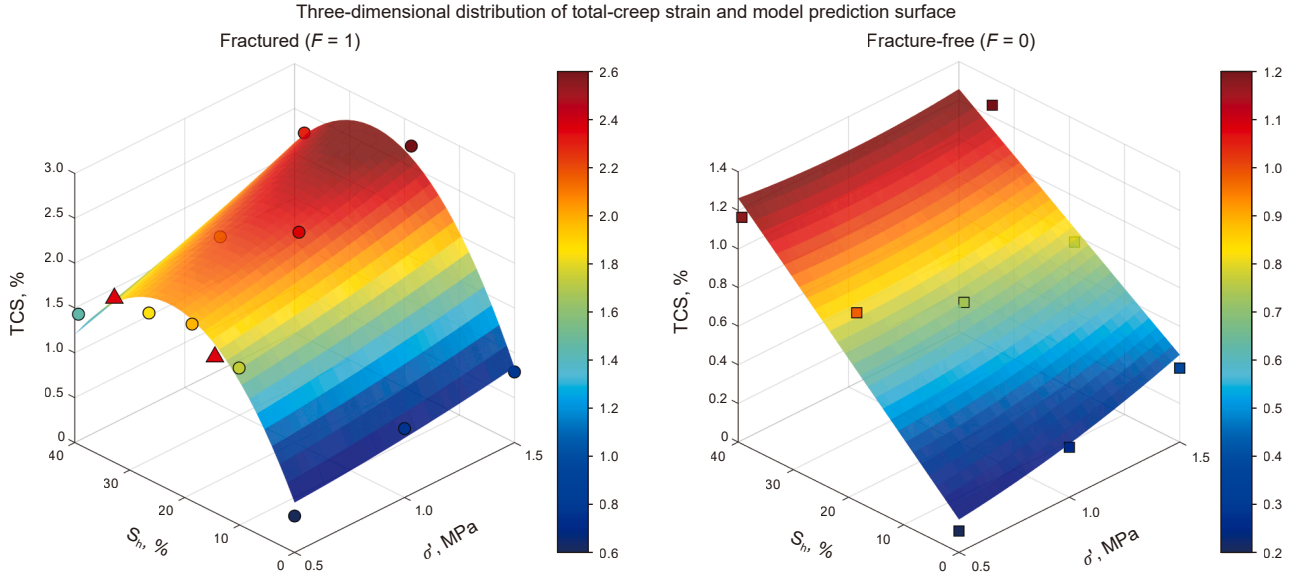


Fig. 33. Three-dimensional distribution of TCS and model prediction surface.

HS. This suggests the existence of a critical saturation, hypothesised to be near an HS of 20%, at which the creep deformation of FHBSs is maximised. We increased the HS values of the test groups by approximately 10%, 15%, 25% and 30% at an ECP of 0.5 MPa to further verify this hypothesis. The corresponding test parameters are shown in Table 3.

Figs. 29 and 30 show the deviatoric stress-strain curves and the creep curves for these FHBSs, respectively. The stress-strain curves in Fig. 29 confirm that the failure strength of the FHBSs increases monotonically with HS, which is consistent with our previous findings (Wang et al., 2025b).

Fig. 31 plots the TCS of the FHBSs as a curve of HS, including the additional data points. The results confirm that the TCS increases to a maximum value at an HS of 18.66% before decreasing. This confirms the existence of a critical saturation around which the relationship between TCS and HS inverts. The competing mechanisms governing this behaviour, similar to those discussed in section 3.1, can be summarised as follows: (1) When HS is less than the critical saturation: In this regime, three factors contribute to increasing creep strain as HS rises. Firstly, the specimen's failure strength increases, necessitating a higher constant creep load (Wang et al., 2025b). Secondly, the initial formation of hydrate is non-uniform due to fractures, creating a heterogeneous stress distribution and a brittle, incomplete cementation network that is susceptible to damage. Thirdly, the formation of NGHs absorbs the water in FHBSs, thereby enabling the generation of large pores (Wu et al., 2018). These combined effects lead to a net decrease in the overall deformation resistance of the FHBSs. (2) When HS is equal to the critical saturation: At this point, the proportion of factors contributing to increased deformation resistance begins to

rise. From this saturation onwards, the deformation resistance of the FHBSs starts to be enhanced. (3) When HS is greater than the critical saturation: As HS increases further, the fracture-filling hydrate becomes progressively denser, and the distribution of hydrate at non-fracture sites becomes more homogeneous (Li et al., 2018). The resulting hydrate network, having achieved a certain scale, provides good support for the FHBSs, which enhances their overall deformation resistance. A schematic diagram illustrating this is shown in Fig. 32.

3.5. Mathematical model

3.5.1. Creep strain model

In this section, MATLAB software was used to fit the experimental data for TCS and ACS from both FHBSs and FFHBSs (excluding the conditions in Table 4). The aim was to derive a multivariable quadratic polynomial equation capable of describing these parameters for both sediment types. The results of these statistical fits are shown in Figs. 33 and 34. For the model, HS and ECP were used as continuous independent variables, while a fracture determination factor F was used as a categorical variable. The TCS or ACS served as the dependent variable. The factor F was defined as 1 for FHBSs and 0 for FFHBSs. The resulting regression equations for TCS and ACS are given in Eq. (4) and Eq. (5), respectively. The model for TCS yielded a mean error of 0.108, a mean squared error of 0.13, and an R^2 of 0.969. The model for ACS yielded a mean error of 0.097, a mean squared error of 0.014 and an R^2 of 0.970. These empirical equations can be used to predict the TCS and ACS of both FHBSs and FFHBSs for a stress ratio R_c of 0.6 under various operational conditions. According to the investigation, stress ratio R_c of 0.6 is more in line with real engineering (Wang et al., 2024a; Yoshimoto and Kimoto, 2022; Zhu et al., 2020). We used this model to calculate the calculated values of other working conditions and compared them with the

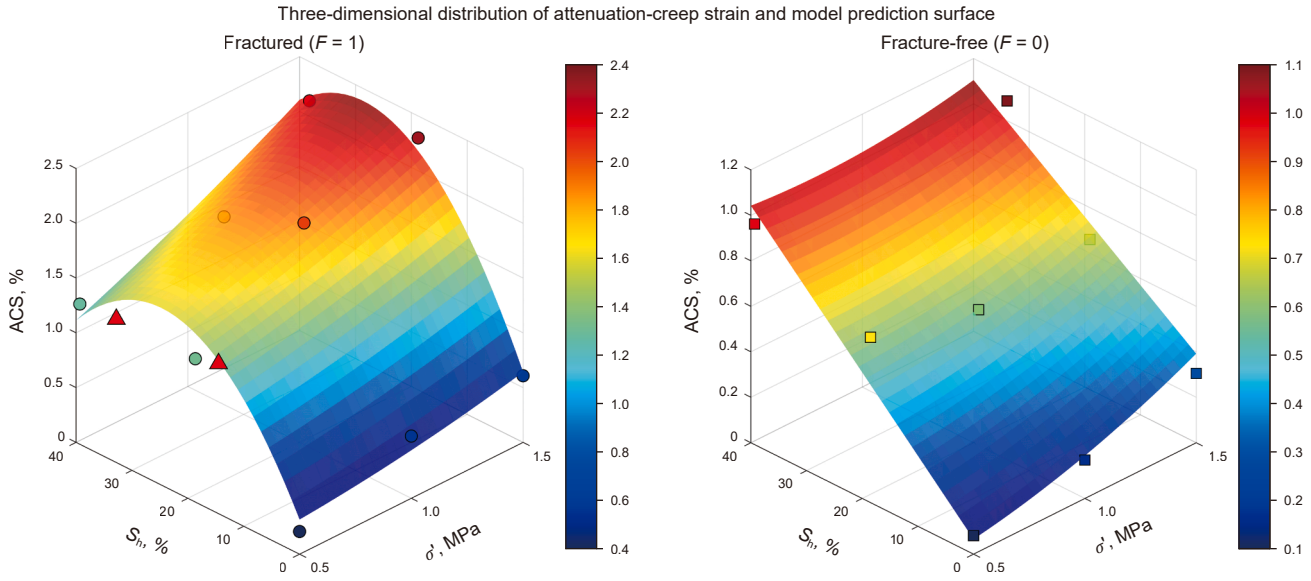


Fig. 34. Three-dimensional distribution of ACS and model prediction surface.

Table 5
Model parameter fitting results.

Specimen type	σ', MPa	S_h, %	q_c, MPa	q_c/E	n, h^{-1}	η, MPa/h	A, h^{-m}	m	t_a, h
Fractured	0.5	0	0.73	0.156	3.841	0.0043	0.0356	0.534	9.699
		10.10	2.24	1.020	1.095	0.0088	0.0274	0.912	10.432
		14.50	2.35	0.975	1.415	0.0095	0.0225	0.555	11.017
		18.66	2.41	1.024	1.122	0.0172	0.0218	0.827	11.628
		26.50	2.59	1.111	0.973	0.0092	0.0171	0.537	17.768
		32.80	2.59	1.024	0.502	0.0073	0.0091	0.785	21.133
		39.33	2.6	0.884	0.516	0.0052	0.0025	1.083	26.874
	1.0	0	1.42	0.429	2.424	0.0035	0.0206	0.545	10.54
		19.21	3.14	1.263	1.068	0.0097	0.0071	1.052	27.223
		33.52	3.38	1.192	0.612	0.0043	0.0010	1.411	38.96
	1.5	0	2.01	0.446	2.284	0.0025	0.0108	0.739	19.487
		18.77	3.16	1.646	0.491	0.0092	0.0064	1.100	28.926
		38.23	3.68	1.429	0.501	0.0045	0.0001	2.406	46.101
Fracture-free	0.5	0	0.74	0.049	7.510	0.0067	0.0107	0.403	5.698
		18.51	2.66	0.448	1.010	0.0148	0.0088	0.597	18.276
		39.33	3.03	0.536	0.984	0.0061	0.0072	0.797	30.855
	1.0	0	1.40	0.115	5.526	0.0070	0.0041	0.566	6.067
		19.09	2.96	0.404	1.286	0.0104	0.0035	0.667	21.19
		40.48	3.41	0.591	0.861	0.0044	0.0021	0.854	31.47
	1.5	0	2.11	0.197	2.457	0.0041	0.0013	0.877	14.767
		19.09	3.21	0.454	1.161	0.0095	0.0011	1.010	22.278
		33.98	3.66	0.625	0.841	0.0029	0.0009	1.253	37.75

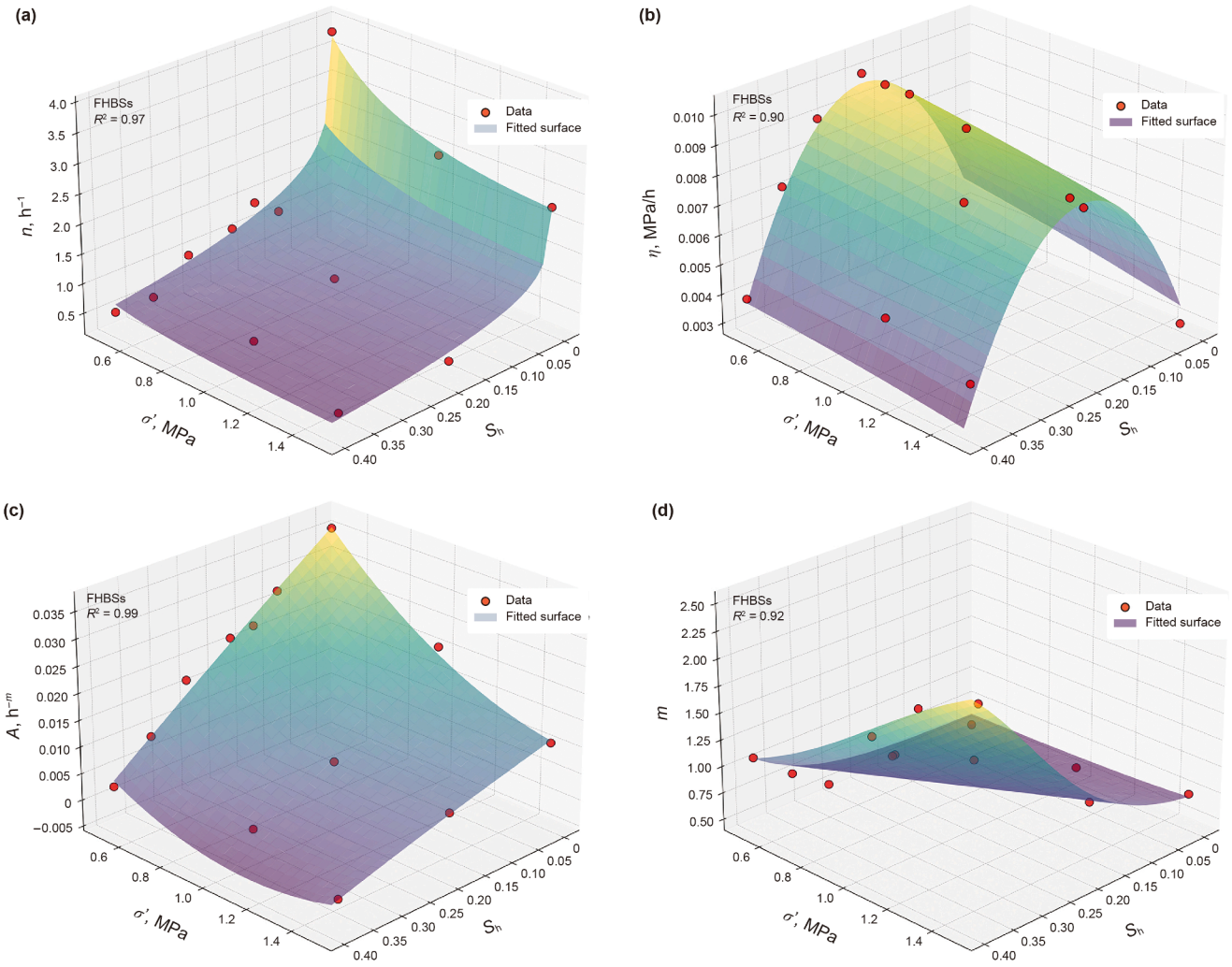


Fig. 35. FHBSs parameter fitting relationship: **(a)** n is related to S_h and σ'; **(b)** η is related to S_h and σ'; **(c)** A is related to S_h and σ'; **(d)** m is related to S_h and σ'.

experimental data, as shown in Table 4. Meanwhile, these working conditions are displayed in triangles in Fig. 33. Obviously, the predictive ability of this model has been confirmed. Such predictive models can help to estimate the deformation capacity of a reservoir during NGH extraction, this provides theoretical guidance for the engineering geological issues involved in the exploitation of natural gas hydrates, thereby aiding in the assessment of extraction risks and the optimisation of production schemes.

$$\begin{aligned}\mathrm{TCS} = {} & 0.13514 + 0.03091 \cdot S_h + 0.38611 \cdot F - 0.0071867 \cdot \sigma' \cdot S_h \\ & + 0.094202 \cdot S_h \cdot F + 0.14097 \cdot \sigma'^2 + 0.023063 \cdot \sigma' \cdot S_h \cdot F \\ & - 0.0029212 \cdot {S_h}^2 \cdot F\end{aligned} \tag{4}$$

$$\begin{aligned}\mathrm{ACS} = {} & 0.02525 + 0.02771 \cdot S_h + 0.25049 \cdot F - 0.0065832 \cdot \sigma' \cdot S_h \\ & + 0.069413 \cdot S_h \cdot F + 0.16287 \cdot \sigma'^2 + 0.023264 \cdot \sigma' \cdot S_h \cdot F \\ & - 0.0021379 \cdot {S_h}^2 \cdot F\end{aligned} \tag{5}$$

However, this model has limitations before it can be widely applied. Currently, it may only be applicable to our experimental conditions. We have proposed this and will gradually improve it in the future.

3.5.2. Time-dependent constitutive model

In this paper, we propose a time-dependent constitutive model to describe the creep behaviour of FHBSs and FFHBSs. We respectively adopt the simplified form of the generalized Kelvin-Voigt model to fit the curves of the attenuation-creep stage, and adopt the simplified form of the Bailey-Norton model to fit the curves of the steady-creep stage (Li et al., 2025a; Sun et al., 2024), and incorporate the influence of hydrate saturation and effective confining pressure on each parameter, as shown in Eqs. (6)–(8).

$$\varepsilon(t) = \begin{cases} \varepsilon_a(t) & t < t_a \\ \varepsilon_a(t) \cdot t + \varepsilon_s(t) & t > t_a \end{cases} \tag{6}$$

$$\varepsilon_a(t) = \frac{q_c}{E} \cdot [1 - \exp(-n \cdot t)] + \eta \cdot \sigma \cdot t \tag{7}$$

$$\varepsilon_s(t) = A \cdot (t - t_a)^m \tag{8}$$

Among them, $\varepsilon(t)$ is the creep variable, $\varepsilon_a(t)$ is the attenuated creep variable, $\varepsilon_s(t)$ is the steady-state creep variable, q_c is the constant load, E is the elastic modulus, n is the attenuation rate, η is the viscosity coefficient, A is the steady-creep coefficient, m is the time index of steady-creep stage, and t_a is the attenuation creep time. The slope between the first two data points in the initial stage of the creep curve is selected as the elastic modulus E. To

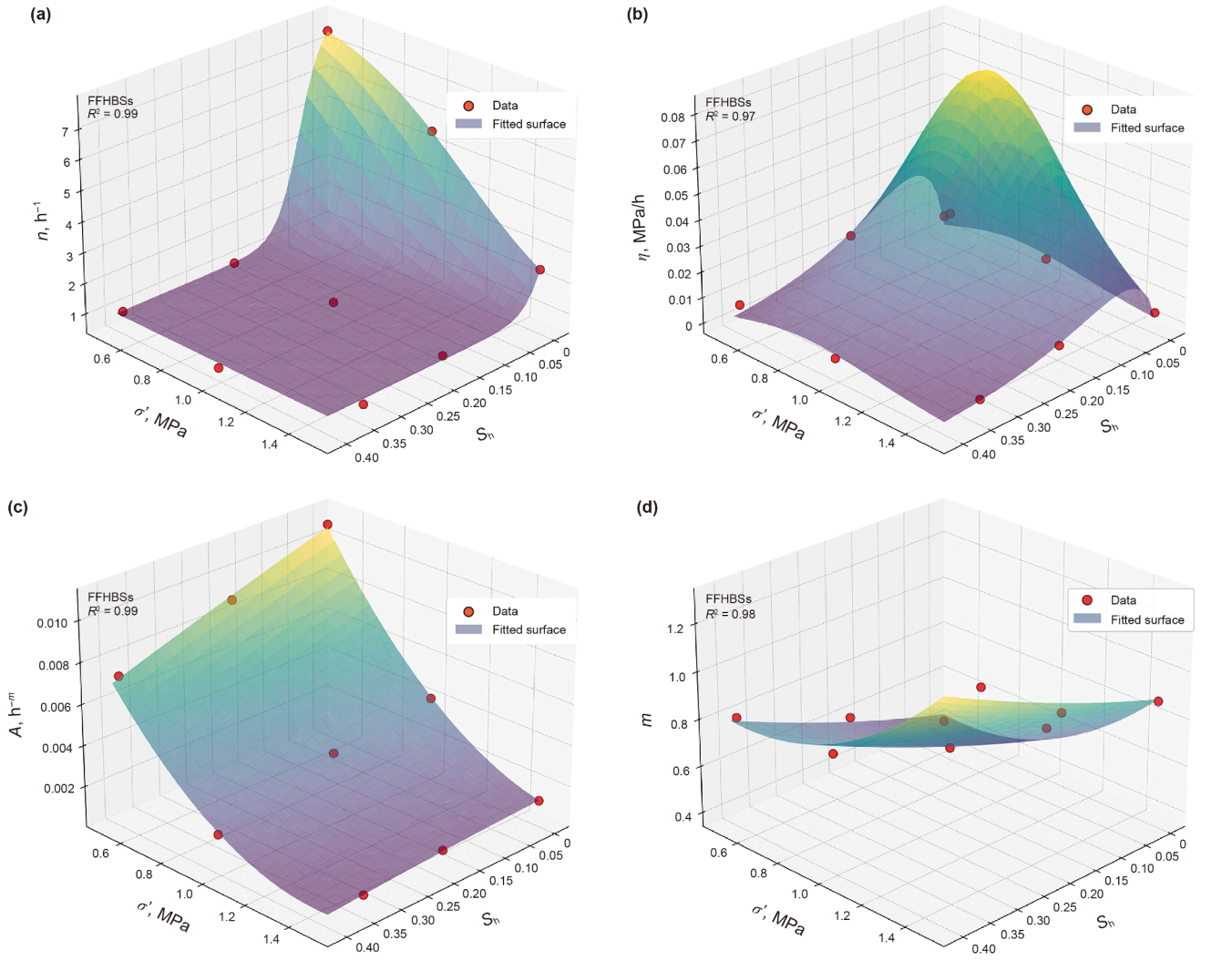


Fig. 36. FFHBSs parameter fitting relationship: **(a)** n is related to S_h and σ'; **(b)** η is related to S_h and σ'; **(c)** A is related to S_h and σ'; **(d)** m is related to S_h and σ'.

Table 6
Model parameter n fitting results.

Specimen type	a_0	a_1	a_2	a_3	a_4
Fractured	0.438	−1.772	0.532	−0.178	−0.950
Fracture-free	1.019	7.008	−44.541	0.092	−3.884

Table 7
Model parameter η fitting results.

Specimen type	b_0	b_1	b_2	b_3	b_4	b_5
Fractured	0.006	0.049	−0.001	−0.136	−0.0002	0.002
Fracture-free	0.020	1.002	−0.541	−0.211	−0.001	0.010

Table 8
Model parameter A fitting results.

Specimen type	c_0	c_1	c_2	c_3	c_4	b_5
Fractured	0.061	−0.104	−0.059	−0.010	0.017	0.052
Fracture-free	0.020	−0.012	−0.023	−0.002	0.007	0.008

Table 9
Model parameter m fitting results.

Specimen type	d_0	d_1	d_2	d_3	d_4	d_5
Fractured	0.711	0.256	−1.102	0.104	0.235	0.031
Fracture-free	0.639	0.631	−0.692	0.529	0.571	0.085

determine the other parameters, nonlinear least squares fitting was performed on the experimental creep curves obtained from FHBSs and FFHBSs under different hydrate saturation (S_h) and effective confining pressure (σ') conditions. This process employed an iterative optimisation algorithm, minimizing the sum of squared residuals between the model predictions and the experiment data, to obtain a set of optimal parameters for each curve, as shown in Table 5.

To further reveal the macroscopic variation patterns of model parameters and their dependence on geological conditions, after obtaining the fitting parameters of all experiments, a second-stage statistical analysis is conducted. In this stage, each parameter (n, η, A, m) is regarded as the dependent variable, while S_h and σ' are taken as the independent variables, and a systematic bivariate regression analysis is carried out. By trying and comparing various

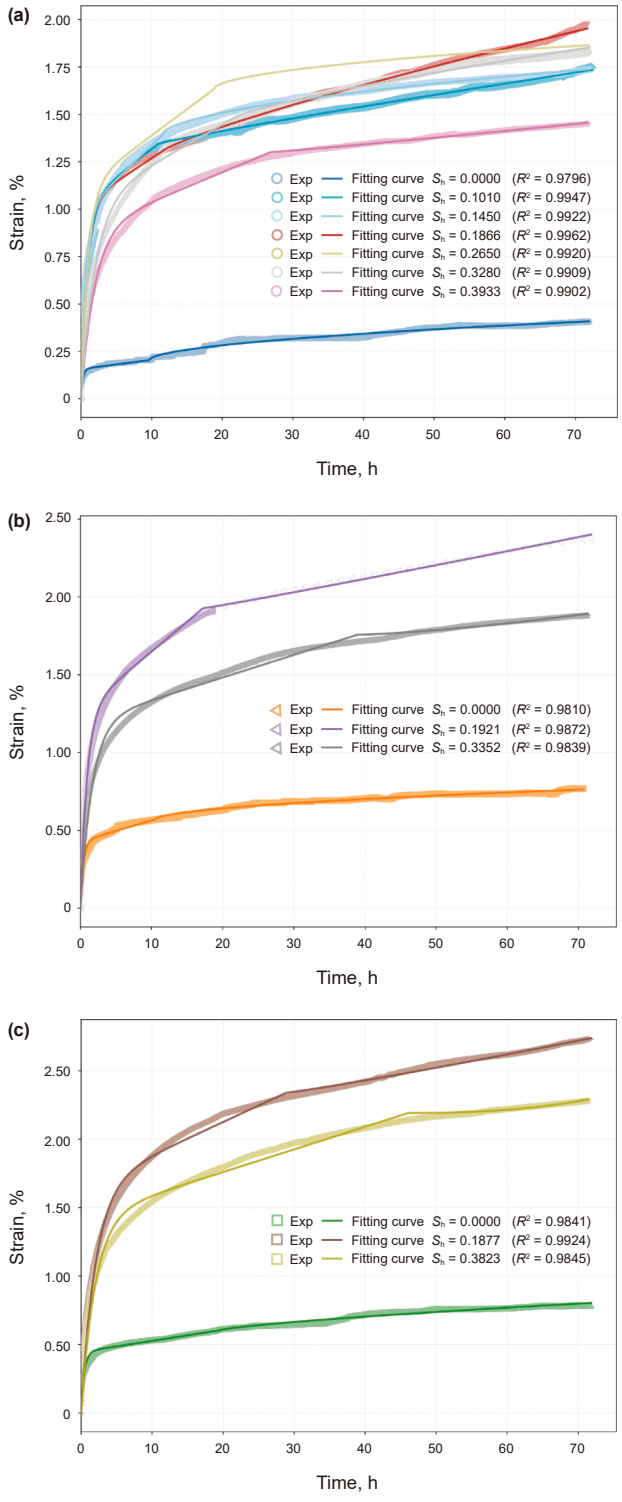


Fig. 37. Comparison of FHBSs experimental data and fitting curves at various hydrate saturations (S_h) under ECPs (σ') of **(a)** 0.5 MPa; **(b)** 1.0 MPa; **(c)** 1.5 MPa.

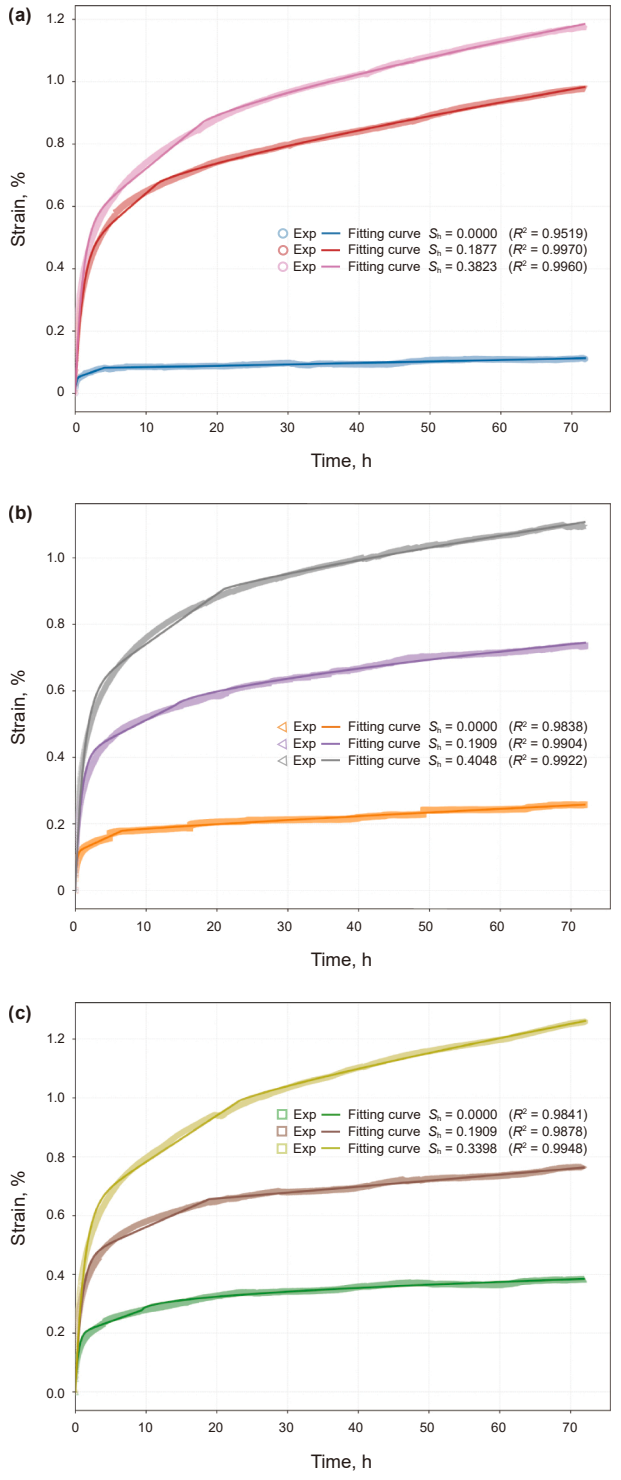


Fig. 38. Comparison of FFHBSs experimental data and fitting curves at various hydrate saturations (S_h) under ECPs (σ') of **(a)** 0.5 MPa; **(b)** 1.0 MPa; **(c)** 1.5 MPa.

empirical models including linear, quadratic, power-law, and exponential functions, based on statistical indicators such as the coefficient of determination (R^2), the best empirical formula that can most accurately describe the relationship of each parameter with S_h and σ' is selected. The parameter n is fitted by Eq. (9), which describes the quantitative relationship between n, S_h and σ'. The optimized fitting graphs of FHBSs and FFHBSs are shown in Figs. 35(a) and 36(a) respectively. The parameters are listed in Table 6.

$$n = a_0 + a_1 / [1 + \exp(a_2 \cdot (S_h + a_3) + a_4 \cdot (S_h + a_3))] \quad (9)$$

The parameter η is fitted by Eq. (10), which describes the quantitative relationship between η, S_h and σ'. The optimized fitting graphs of FHBSs and FFHBSs are shown in Figs. 35(b) and 36(b) respectively. The parameters are listed in Table 7.

$$\eta = b_0 + b_1 \cdot S_h + b_2 \cdot \sigma' + b_3 \cdot {S_h}^2 + b_4 \cdot \sigma'^2 + b_5 \cdot S_h \cdot \sigma' \quad (10)$$

The parameter A is fitted by Eq. (11), which describes the quantitative relationship between A, S_h and σ'. The optimized fitting graphs of FHBSs and FFHBSs are shown in Figs. 35(c) and 36(c) respectively. The parameters are listed in Table 8.

$$A = c_0 + c_1 \cdot S_h + c_2 \cdot \sigma' + c_3 \cdot {S_h}^2 + c_4 \cdot \sigma'^2 + c_5 \cdot S_h \cdot \sigma' \quad (11)$$

The parameter m is fitted by Eq. (12), which describes the quantitative relationship between m, S_h and σ'. The optimized fitting graphs of FHBSs and FFHBSs are shown in Figs. 35(d) and 36(d) respectively. The parameters are listed in Table 9.

$$m = d_0 + d_1 \cdot S_h + d_2 \cdot \sigma' + d_3 \cdot {S_h}^2 + d_4 \cdot \sigma'^2 + d_5 \cdot S_h \cdot \sigma' \quad (12)$$

In Figs. 37 and 38, the solid lines represent the fitting results, while the scattered points correspond to the experimental data. It is worth noting that the correlation coefficients of the model fitting all reached values above 0.98. This strong correlation indicates that the parameters in Table 5 effectively represent the creep behaviour of FHBSs and FFHBSs at different hydrate saturations and effective confining pressures.

4. Conclusion

In this study, the creep properties of FHBSs and FFHBSs were investigated under various ECPs and HS. The influences of HS and ECP on key creep parameters, TCS, ACS, ACR, RR, and RIT were analysed. A direct comparison of these properties between the two specimen types was also conducted, and the existence of a critical saturation for the creep of FHBSs was investigated and confirmed. The main conclusions are as follows:

(1) The presence of fractures dictates the sediment's response to hydrate saturation. For FHBSs, the TCS, ACS, ACR, and RR exhibit a non-monotonic trend, initially increasing and then decreasing with rising HS. In contrast, these parameters for FFHBSs are all positively correlated with HS. The ACRs for FHBSs with 20% and 40% HS converge at higher ECPs (e.g., 1.5 MPa), a phenomenon not observed in FFHBSs.
(2) For both specimen types, the RIT increases with increasing HS and ECP.
(3) The presence of fractures consistently results in higher TCS and ACS in FHBSs compared to FFHBSs. The RR of FHBSs is also larger than that of FFHBSs under most conditions.
(4) A critical HS exists for FHBSs at approximately 20% HS, at which the TCS peaks. Below this critical saturation, TCS increases with HS; above it, TCS decreases with increasing HS.
(5) Empirical multivariable quadratic polynomial equations were developed using linear regression to model the TCS and ACS for both FHBSs and FFHBSs as a function of ECP and HS. These models can be used to predict reservoir deformation during NGH extraction, thereby aiding in risk assessment and the optimisation of production schemes.

This study has focused on investigating the creep behaviour of FHBSs. The conclusions drawn from this study can provide theoretical basis for the geological safety of fractured reservoirs during the NGH extraction process. In the future, our work will focus on the creep characteristics of FHBSs under different fracture roughness and stress ratios, increase the data volume and creep duration, and continuously improve the existing mathematical model to achieve promotion and enhance practical application value. In addition, we will comprehensively consider the synergistic effects of temperature changes and hole pressure variations during heating and depressurization mining as well as different stress paths. Moreover, we will conduct in-situ CT triaxial creep experiments to achieve in-situ, real-time and high-resolution visualization observation of the internal microstructure of fractured hydrate-bearing sediments, and obtain more reliable explanations of the rheological mechanisms. Finally, we will conduct a more comprehensive and systematic study on the mechanical properties of fractured hydrate sediments by combining multiple thermal-water-mechanical-chemical coupled numerical simulations. These future studies will enable a more in-depth and comprehensive investigation into the engineering geological issues involved in the extraction of natural gas hydrates.

CRediT authorship contribution statement

Lei Wang: Writing – review & editing, Funding acquisition. **Jia-Hao Yu:** Writing – original draft. **Kai Zhang:** Writing – original draft. **Zhi-Heng Liu:** Investigation. **Wen-Qi Yu:** Investigation. **Zhao-Ran Wu:** Resources. **Jing-Yan Lan:** Investigation. **Qiang Wang:** Investigation. **Bing-Bing Chen:** Investigation.

Declaration of competing interest

The authors declare that they have no known competing financial interests or personal relationships that could have appeared to influence the work reported in this paper.

Acknowledgment

This study was financially supported by the National Natural Science Foundation of China (Grant Nos. 42306241, 42406228), Hebei Natural Science Foundation (D2025203001). We would like to thank MogoEdit (https://www.mogoedit.com) for its English editing during the preparation of this manuscript.

References

ASTM, D., 2017. 2487, standard practice for classification of soils for engineering purposes 426 (unified soil classification system). Annu. Book ASTM (Am. Soc. Test. Mater.) Stand, pp. 2. USA.
Cai, J., Xia, Y., Lu, C., et al., 2020. Creeping microstructure and fractal permeability model of natural gas hydrate reservoir. Mar. Petrol. Geol. 115, 104282. https://doi.org/10.1016/j.marpetgeo.2020.104282.
Cameron, I., Handa, Y.P., Baker, T.H.W., 1990. Compressive strength and creep behavior of hydrate-consolidated sand. Can. Geotech. J. 27, 255–258. https://doi.org/10.1139/t90-030.
Chen, B., Chen, J., Wu, M., et al., 2026. Pressure and multiphase flow effects on CO_2 storage in hydrate-based cap: a comprehensive analysis. Int. J. Heat Mass Tran. 256, 127960. https://doi.org/10.1016/j.ijheatmasstransfer.2025.127960.
Chen, M., Li, Y., Zhang, Y., et al., 2023. Recent advances in creep behaviors characterization for hydrate-bearing sediment. Renew. Sustain. Energy Rev. 183, 113434. https://doi.org/10.1016/j.rser.2023.113434.
Chen, P., Xu, J., Fan, Q., et al., 2025. Shear strength behavior of hydrate-bearing sediments under varying dissociation conditions. J. Rock Mech. Geotech. Eng. 17, 3819–3832. https://doi.org/10.1016/j.jrmge.2025.02.001.
Chuvilin, E.M., Bukhanov, B.A., Grebenkin, S.I., et al., 2018. Shear strength of frozen sand with dissociating pore methane hydrate: an experimental study. Cold Reg. Sci. Technol. 153, 101–105. https://doi.org/10.1016/j.coldregions.2018.04.013.
Cook, A.E., Goldberg, D., 2008. Extent of gas hydrate filled fracture planes: implications for *in situ* methanogenesis and resource potential. Geophys. Res. Lett. 35. https://doi.org/10.1029/2008GL034587.
Dong, L., Wu, N., Liu, F., et al., 2024. Estimation on strength parameters of sediments with hydrate layered distribution based on triaxial shearing tests. Gas Sci. Eng. 123, 205255. https://doi.org/10.1016/j.jgsce.2024.205255.
Dong, L., Li, Y., Liao, H., et al., 2020. Strength estimation for hydrate-bearing sediments based on triaxial shearing tests. J. Petrol. Sci. Eng. 184, 106478. https://doi.org/10.1016/j.petrol.2019.106478.
Du, H., Chen, H., Wang, Q., et al., 2023. Mechanical behavior of reservoirs with heterogeneous hydrate distribution: analysis from the thickness and angle of the hydrate-bearing layer. Eng. Geol. 327, 107359. https://doi.org/10.1016/j.enggeo.2023.107359.

Du, Y., Li, T., Li, W., et al., 2020. Experimental study of mechanical and permeability behaviors during the failure of sandstone containing two preexisting fissures under triaxial compression. Rock Mech. Rock Eng. 53, 3673–3697. https://doi.org/10.1007/s00603-020-02119-x.
Durham, W.B., Kirby, S.H., Stern, L.A., et al., 2003. The strength and rheology of methane clathrate hydrate. J. Geophys. Res. Solid Earth 108. https://doi.org/10.1029/2002JB001872.
Exley, R.J.K., Westbrook, G.K., Haacke, R.R., et al., 2010. Detection of seismic anisotropy using ocean bottom seismometers: a case study from the northern headwall of the Storegga Slide. Geophys. J. Int. 183, 188–210. https://doi.org/10.1111/j.1365-246X.2010.04730.x.
Gabitto, J.F., Tsouris, C., 2010. Physical properties of gas hydrates: a review. J. Thermodynam. 2010, 271291. https://doi.org/10.1155/2010/271291.
Hiruta, A., Matsumoto, R., 2022. Massive gas hydrates buried on Umitaka Spur in the Sea of Japan: description, origin, and significance to methane cycling in marine sediment. Geo Mar. Lett. 42, 13. https://doi.org/10.1007/s00367-022-00735-w.
Hu, Q., Li, Y., Wu, N., et al., 2023. Study on creep behaviors and nonlinear creep constitutive model for sandy marine hydrate-bearing sediments. Ocean Eng. 286, 115717. https://doi.org/10.1016/j.oceaneng.2023.115717.
Hu, Q., Sun, X., Qu, J., et al., 2025. Creep behaviors of methane hydrate-bearing sandy sediments under load-to-unload stress state. Geoenergy Sci. Eng. 247, 213702. https://doi.org/10.1016/j.geoen.2025.213702.
Huaimin, D., Jianmeng, S., Likai, C., et al., 2018. Study on the effects of natural gas hydrate cementation mode on the physical properties of rocks. J. Geophys. Eng. 15, 1399–1406. https://doi.org/10.1088/1742-2140/aab625.
Jiang, M., Sun, C., Crosta, G.B., et al., 2015. A study of submarine steep slope failures triggered by thermal dissociation of methane hydrates using a coupled CFD-DEM approach. Eng. Geol. 190, 1–16. https://doi.org/10.1016/j.enggeo.2015.02.007.
Lee, M., Collett, T., 2009. Gas hydrate saturations estimated from fractured reservoir at Site NGHP-01-10, Krishna-Godavari Basin, India. J. Geophys. Res. Solid Earth 114. https://doi.org/10.1029/2008JB006237.
Lee, M.W., Collett, T.S., 2013. Characteristics and interpretation of fracture-filled gas hydrate – an example from the Ulleung Basin, East Sea of Korea. Mar. Petrol. Geol. 47, 168–181. https://doi.org/10.1016/j.marpetgeo.2012.09.003.
Li, K., Zhang, F.Q., Yang, B.W., et al., 2025a. Modeling the creep behavior of hydrate-bearing sediments using a variable-order fractal derivative. Can. Geotech. J. 62, 1–10. https://doi.org/10.1139/cgj-2025-0077.
Li, Y., Liu, W., Song, Y., et al., 2016. Creep behaviors of methane hydrate coexisting with ice. J. Nat. Gas Sci. Eng. 33, 347–354. https://doi.org/10.1016/j.jngse.2016.05.042.
Li, Y., Cheng, Y., Yan, C., et al., 2023a. Triaxial creep tests and the visco-elastic-plastic constitutive model of hydrate formations. Gas Sci. Eng. 115, 205006. https://doi.org/10.1016/j.jgsce.2023.205006.
Li, Y., Xin, X., Xu, T., et al., 2023b. Production behavior of hydrate-bearing sediments with mixed Fracture- and pore-filling hydrates. J. Mar. Sci. Eng. 11 (7), 1321. https://doi.org/10.3390/jmse11071321.
Li, Y., Dong, L., Wu, N., et al., 2021. Influences of hydrate layered distribution patterns on triaxial shearing characteristics of hydrate-bearing sediments. Eng. Geol. 294, 106375. https://doi.org/10.1016/j.enggeo.2021.106375.
Li, S.L., Sun, Y.H., Su, K., et al., 2018. Numerical simulation of CH4 hydrate formation in fractures. Energy Explor. Exploit. 36, 1279–1294. https://doi.org/10.1177/0144598717751180.
Li, Y., Wang, L., Xie, Y., et al., 2023c. Deformation characteristics of methane hydrate-bearing clayey and sandy sediments during depressurization dissociation. Energy 275, 127527. https://doi.org/10.1016/j.energy.2023.127527.
Li, Y., Chen, M., Zhang, Y., et al., 2024. Time-dependent deformation of marine gas hydrate-bearing strata conditioned to a wellbore: experiments and implications. Ocean Eng. 308, 118220. https://doi.org/10.1016/j.oceaneng.2024.118220.
Li, Y., Xin, X., Liu, M., et al., 2025b. An experimental study on gas-liquid phase fluid migration in hydrate-bearing sediments during hydrate dissociation. Eng. Geol., 108163 https://doi.org/10.1016/j.enggeo.2025.108163.
Li, Y., Yu, G., Xu, M., et al., 2022. Interfacial strength between ice and sediment: a solution towards fracture-filling hydrate system. Fuel 330, 125553. https://doi.org/10.1016/j.fuel.2022.125553.
Liu, A., Kwok, C., Li, W., et al., 2023a. Strain rate effects on intact deep-sea sediments under different confining pressures and overconsolidation ratios. Eng. Geol. 327, 107357. https://doi.org/10.1016/j.enggeo.2023.107357.
Liu, F., Tan, L., Crosta, G., et al., 2020. Spatiotemporal destabilization modes of upper continental slopes undergoing hydrate dissociation. Eng. Geol. 264, 105286. https://doi.org/10.1016/j.enggeo.2019.105286.
Liu, T., Wu, P., Lu, Q., et al., 2024. Creep and wave velocity characterization on anisotropic consolidated methane hydrate sediments of the South China Sea. Energy Fuel. 38, 16416–16425. https://doi.org/10.1021/acs.energyfuels.4c02845.
Liu, T., Tang, H., Wu, P., et al., 2023b. Acoustic characteristics on clayey-silty sediments of the South China Sea during methane hydrate formation and dissociation. Energy 282, 128978. https://doi.org/10.1016/j.energy.2023.128978.
Liu, W., Song, Q., Wu, P., et al., 2023c. Triaxial tests on anisotropic consolidated methane hydrate-bearing clayey-silty sediments of the South China Sea. Energy 284, 129260. https://doi.org/10.1016/j.energy.2023.129260.
Liu, Z., Kim, J., Hu, G., et al., 2021. Geomechanical property evolution of hydrate-bearing sediments under dynamic loads: nonlinear behaviors of modulus and damping ratio. Eng. Geol. 295, 106427. https://doi.org/10.1016/j.enggeo.2021.106427.
Nakashima, K., Nakata, Y., Hyodo, M., et al., 2021. Compressive characteristics of methane hydrate-bearing sands under isotropic consolidation. Soils Found. 61, 506–519. https://doi.org/10.1016/j.sandf.2021.01.011.
Peng, C., Zou, C., Lu, Z., et al., 2019. Evidence of pore-and fracture-filling gas hydrates from geophysical logs in consolidated rocks of the Muli area, Qinghai-Tibetan Plateau Permafrost, China. J. Geophys. Res. Solid Earth 124, 6297–6314. https://doi.org/10.1029/2018JB016041.
Priest, J.A., Hayley, J.L., 2019. Strength of laboratory synthesized hydrate-bearing sands and their relationship to natural hydrate-bearing sediments. J. Geophys. Res. Solid Earth 124, 12556–12575. https://doi.org/10.1029/2019JB018324.
Radjai, F., Wolf, D.E., Jean, M., et al., 1998. Bimodal Character of stress transmission in granular packings. Phys. Rev. Lett. 80, 61–64. https://doi.org/10.1103/PhysRevLett.80.61.
Riedel, M., Collett, T.S., Kumar, P., et al., 2010. Seismic imaging of a fractured gas hydrate system in the Krishna-Godavari Basin offshore India. Mar. Petrol. Geol. 27, 1476–1493. https://doi.org/10.1016/j.marpetgeo.2010.06.002.
Sang, S., Kong, L., Zeng, Z., et al., 2025. The shear characterization of hydrate-bearing clayey-silty sediments with layered hydrate distributions: insights from different hydrate saturations and effective confining pressures. Soil Dynam. Earthq. Eng. 192, 109289. https://doi.org/10.1016/j.soildyn.2025.109289.
Sassen, R., Losh, S.L., Cathles, L., et al., 2001. Massive vein-filling gas hydrate: relation to ongoing gas migration from the deep subsurface in the Gulf of Mexico. Mar. Petrol. Geol. 18, 551–560. https://doi.org/10.1016/S0264-8172(01)00014-9.
Sun, L., Sun, H., Yuan, C., et al., 2023. Enhanced clathrate hydrate formation at ambient temperatures (287.2 K) and near atmospheric pressure (0.1 MPa): application to solidified natural gas technology. Chem. Eng. J. 454, 140325. https://doi.org/10.1016/j.cej.2022.140325.
Sun, S., Zhang, X., Zhou, Y., 2024. Features and constitutive model of hydrate-bearing sandy sediment's triaxial creep failure. Water 16 (20), 2947. https://doi.org/10.3390/w16202947.
Tan, L., Liu, F., Huang, Y., et al., 2021. Production-induced instability of a gentle submarine slope: potential impact of gas hydrate exploitation with the huff-puff method. Eng. Geol. 289, 106174. https://doi.org/10.1016/j.enggeo.2021.106174.
Wang, H., Wu, P., Li, Y., et al., 2023. Gas permeability variation during methane hydrate dissociation by depressurization in marine sediments. Energy 263, 125749. https://doi.org/10.1016/j.energy.2022.125749.
Wang, L., Shen, S., Wu, Z., et al., 2024. Strength and creep characteristics of methane hydrate-bearing clayey silts of the South China Sea. Energy 294, 130789. https://doi.org/10.1016/j.energy.2024.130789.
Wang, L., Liu, Z., Yan, X., et al., 2025a. Stress-strain and creep behaviors of marine overconsolidated hydrate-bearing sediments. Geoenergy Sci. Eng. 254, 214036. https://doi.org/10.1016/j.geoen.2025.214036.
Wang, L., Li, Y., Wu, P., et al., 2020. Physical and mechanical properties of the overburden layer on gas hydrate-bearing sediments of the South China sea. J. Petrol. Sci. Eng. 189, 107020. https://doi.org/10.1016/j.petrol.2020.107020.
Wang, L., Yu, W., Zhang, K., et al., 2025b. Strength characteristics of fractured methane hydrate-bearing sediments. Eng. Fract. Mech. 319, 110986. https://doi.org/10.1016/j.engfracmech.2025.110986.
Wei, D., Jinqiang, L., Wei, Z., et al., 2021. Typical characteristics of fracture-filling hydrate-charged reservoirs caused by heterogeneous fluid flow in the Qiongdongnan Basin, northern south China sea. Mar. Petrol. Geol. 124, 104810. https://doi.org/10.1016/j.marpetgeo.2020.104810.
Wei, R., Liu, L., Jia, C., et al., 2023. Undrained triaxial shear tests on hydrate-bearing fine-grained sediments from the shenhu area of South China Sea. J. Mar. Sci. Eng. 11 (8), 1604. https://doi.org/10.3390/jmse11081604.
Wu, P., Li, Y., Wang, L., et al., 2022. Hydrate-bearing sediment of the South China Sea: microstructure and mechanical characteristics. Eng. Geol. 307, 106782. https://doi.org/10.1016/j.enggeo.2022.106782.
Wu, Z., Li, Y., Sun, X., et al., 2018. Experimental study on the gas phase permeability of montmorillonite sediments in the presence of hydrates. Mar. Petrol. Geol. 91, 373–380. https://doi.org/10.1016/j.marpetgeo.2018.01.015.
Wu, Z., Zhang, K., Ma, S., et al., 2025. Effect of nano-surface on water flow in methane hydrate montmorillonite reservoir: a molecular dynamics study. Geoenergy Sci. Eng. 250, 213826. https://doi.org/10.1016/j.geoen.2025.213826.
Xu, J., Xu, C., Huang, L., et al., 2023. Strength estimation and stress–dilatancy characteristics of natural gas hydrate-bearing sediments under high effective confining pressure. Acta Geotech. 18, 811–827. https://doi.org/10.1007/s11440-022-01620-7.
Yang, M., Song, W., Zhang, L., et al., 2026. Evaluation of carbon sequestration stability based on ice-hydrate coupling effect in ice lenses covered permafrost regions. Int. J. Min. Sci. Technol. https://doi.org/10.1016/j.ijmst.2026.01.007.
Yang, Y., Lai, Y., Chang, X., 2010. Experimental and theoretical studies on the creep behavior of warm ice-rich frozen sand. Cold Reg. Sci. Technol. 63, 61–67. https://doi.org/10.1016/j.coldregions.2010.04.011.
Yoshimoto, M., Kimoto, S., 2022. Undrained creep behavior of CO_2 hydrate-bearing sand and its constitutive modeling considering the cementing effect of hydrates. Soils Found. 62, 101095. https://doi.org/10.1016/j.sandf.2021.101095.
You, Z., Hao, Y., Hu, W., et al., 2023. Strength analysis of hydrate-bearing sandy sediments in excess gas and excess water based on drained triaxial compression tests. Eng. Geol. 325, 107292. https://doi.org/10.1016/j.enggeo.2023.107292.

Zhang, C., Luo, T., Yang, W., et al., 2024a. Triaxial tests on hydrate-bearing silty-clayey sediments concerning pore-filling habit. Geoenergy Sci. Eng. 237, 212802. https://doi.org/10.1016/j.geoen.2024.212802.

Zhang, T.T., Wan, Q.C., Li, B., et al., 2025. Exploring the self-preservation effect on gas hydrate dissociation: a comparative analysis of equilibrium and kinetic models in Permafrost area. Energy Fuel. 39, 12523–12537. https://doi.org/10.1021/acs.energyfuels.5c01844.

Zhang, K., Wang, L., Liu, Z., et al., 2024b. Experimental study of permeability characteristics of fracture-hosted hydrate-bearing clay sediments under triaxial shear. Geoenergy Sci. Eng. 241, 213183. https://doi.org/10.1016/j.geoen.2024.213183.

Zhang, L., Liu, H., Shan, X., et al., 2026. Stability assessment of CO_2 hydrate-based sequestration in complex marine environments. Chem. Eng. J. 527, 171826. https://doi.org/10.1016/j.cej.2025.171826.

Zhang, T.T., Li, B., Wei, W.N., et al., 2024c. Kinetic study on the effect of ice nucleation and generation on methane hydrate dissociation below the quadruple point. Gas Sci. Eng. 131, 205468. https://doi.org/10.1016/j.jgsce.2024.205468.

Zhang, W., Ma, Q., Wang, R., et al., 2011. An experimental study of shear strength of gas-hydrate-bearing core samples. Pet. Sci. 8, 177–182. https://doi.org/10.1007/s12182-011-0132-2.

Zhao, Y., Kong, L., Xu, R., et al., 2022. Strength behaviors of hydrate-bearing clayey-silty sediments with multiple factors. J. Petrol. Sci. Eng. 219, 111035. https://doi.org/10.1016/j.petrol.2022.111035.

Zhao, Y., Hu, G., Liu, L., et al., 2025. Mechanical properties of gas hydrate-bearing sediments: research progress, challenges and perspectives. Earth Sci. Rev. 262, 105058. https://doi.org/10.1016/j.earscirev.2025.105058.

Zhou, S., Yang, L., Lv, X., et al., 2021. Fine sand migration in hydrate-bearing sediments and median grain size ratio optimization of gravel pack. J. Nat. Gas Sci. Eng. 88, 103809. https://doi.org/10.1016/j.jngse.2021.103809.

Zhou, W., Wang, Y., Gao, X., et al., 2015. Architecture, evolution history and controlling factors of the Baiyun submarine canyon system from the middle Miocene to Quaternary in the Pearl River Mouth Basin, northern South China Sea. Mar. Petrol. Geol. 67, 389–407. https://doi.org/10.1016/j.marpetgeo.2015.05.015.

Zhou, Y., Zhou, J., Chen, P., et al., 2024. Shear strength degradation of gas hydrate-bearing sediment due to partial hydrate dissociation. J. Rock Mech. Geotech. Eng. 16, 2749–2763. https://doi.org/10.1016/j.jrmge.2023.10.002.

Zhu, Y., Chen, C., Luo, T., et al., 2020. Creep behaviours of methane hydrate-bearing sediments. Environ. Geotechn. 9, 199–209. https://doi.org/10.1680/jenge.18.00196.